J. Fluid Mech. (2019), *vol.* 867, *pp.* 906–933.
doi:10.1017/jfm.2019.119

Resolved and subgrid dynamics of Rayleigh–Bénard convection

Riccardo Togni[1], **Andrea Cimarelli**[2] **and Elisabetta De Angelis**[1,2,†]

[1]DIN, Università di Bologna, Via Fontanelle 40, 47121 Forlì, Italy

[2]School of Engineering, Cardiff University, Queen's Buildings, The Parade, Cardiff CF24 3AA, UK

(Received 11 May 2017; revised 20 October 2018; accepted 5 February 2019;
first published online 28 March 2019)

In this work we present and demonstrate the reliability of a theoretical framework for the study of thermally driven turbulence. It consists of scale-by-scale budget equations for the second-order velocity and temperature structure functions and their limiting cases, represented by the turbulent kinetic energy and temperature variance budgets. This framework represents an extension of the classical Kolmogorov and Yaglom equations to inhomogeneous and anisotropic flows, and allows for a novel assessment of the turbulent processes occurring at different scales and locations in the fluid domain. Two relevant characteristic scales, ℓ_c^u for the velocity field and ℓ_c^θ for the temperature field, are identified. These variables separate the space of scales into a quasi-homogeneous range, characterized by turbulent kinetic energy and temperature variance cascades towards dissipation, and an inhomogeneity-dominated range, where the production and the transport in physical space are important. This theoretical framework is then extended to the context of large-eddy simulation to quantify the effect of a low-pass filtering operation on both resolved and subgrid dynamics of turbulent Rayleigh–Bénard convection. It consists of single-point and scale-by-scale budget equations for the filtered velocity and temperature fields. To evaluate the effect of the filter length ℓ_F on the resolved and subgrid dynamics, the velocity and temperature fields obtained from a direct numerical simulation are split into filtered and residual components using a spectral cutoff filter. It is found that when ℓ_F is smaller than the minimum values of the cross-over scales given by $\ell_{c,min}^{\theta*} = \ell_{c,min}^{\theta} Nu/H = 0.8$, the resolved processes correspond to the exact ones, except for a depletion of viscous and thermal dissipations, and the only role of the subgrid scales is to drain turbulent kinetic energy and temperature variance to dissipate them. On the other hand, the resolved dynamics is much poorer in the near-wall region and the effects of the subgrid scales are more complex for filter lengths of the order of $\ell_F \approx 3\ell_{c,min}^{\theta}$ or larger. This study suggests that classic eddy-viscosity/diffusivity models employed in large-eddy simulation may suffer from some limitations for large filter lengths, and that alternative closures should be considered to account for the inhomogeneous processes at subgrid level. Moreover, the theoretical framework based on the filtered Kolmogorov and Yaglom equations may represent a valuable tool for future assessments of the subgrid-scale models.

Key words: turbulent convection, turbulence modelling, turbulence theory

† Email address for correspondence: e.deangelis@unibo.it

1. Introduction

Since the beginning of computational fluid dynamics, large-eddy simulation (LES) of thermally driven flows has been the subject of many studies, in particular for meteorological applications (Smagorinsky 1963; Lilly 1967; Deardorff 1974). The original motivation was driven by the failure of analytical methods to describe the dynamics of the atmosphere, together with the intrinsic limitations of both experimental measurements and numerical solutions of the full governing equations (Lilly 1962). The computational resources required for a direct numerical simulation (DNS) are still prohibitive nowadays for most engineering and geophysical flows. However, the steady increase of computing power over the last decades has aroused new interest in the LES technique and great effort has been spent to improve its level of feasibility and accuracy (Piomelli 1999).

Correct treatment of the near-wall region represents one of the main challenges in LES because production and transport mechanisms induced by spatial inhomogeneity involve even smaller scales as the boundaries are approached (Porté-Agel *et al.* 2001); hence, the local integral scale of the flow steeply decreases from the bulk to the wall, and such a drop can be of several orders of magnitude in systems of practical interest (Piomelli & Balaras 2002). The result is that the computational cost required by a wall-resolved LES, in terms of CPU time and memory, cannot be afforded in the case of high-Reynolds-number flows. To overcome this limitation, a significant reduction of the near-wall resolution is demanded. In this context, it is fundamental to understand which turbulent mechanisms are going to be captured and which are going to be filtered out by an LES. This is important for two distinct but interrelated reasons. In the first place, a clear overview of the resolved dynamics allows for the identification of a minimum resolution requirement, namely the smallest scale of the flow that we aim to solve numerically in order to capture the structures that are more energetic and less universal (Bryan, Wyngaard & Fritsch 2003). Secondly, the analysis of the subgrid dynamics represents an ideal premise for the formulation of a physically based subgrid-scale (SGS) model capable of reproducing, as best as possible, the effects of the unresolved scales (Mason 1989).

Following this line of research, the main goal of the present paper is to shed light on the resolved and subgrid dynamics of thermally driven turbulence via the analysis of a filtered DNS dataset. This methodology, called *a priori* in LES studies, can serve as an efficient tool for checking to what extent the resolved physics reproduces the real one and how the SGS model copes with the interplay between resolved and subgrid scales. Owing to the inherent complexity of natural and technological flows, we focus our investigation on a canonical system, Rayleigh–Bénard convection (RBC), commonly defined as a fluid layer confined between two infinite horizontal walls, heated from below and cooled from above (Siggia 1994; Chillà & Schumacher 2012). RBC is simple enough to treat by theoretical, numerical and experimental studies, although it preserves the essential features of thermally driven flows, namely the balance between buoyancy force and viscous/diffusive damping (Ahlers *et al.* 2012; Gayen, Hughes & Griffiths 2013). Some studies have been devoted to the assessment of SGS models for RBC (Cabot 1993; Kimmel & Domaradzki 2000; Sergent, Joubert & Le Quéré 2006; Dabbagh *et al.* 2016, 2017); however, the literature lacks a detailed *a priori* analysis of this system, unlike other paradigmatic flows such as the round jet (Liu, Meneveau & Katz 1994), the transitional (Piomelli *et al.* 1991) and the stationary channel flows (Härtel *et al.* 1994).

The identification of the local integral scales in RBC is presented in the first part of this work. For this purpose, a DNS dataset at Rayleigh number $Ra = 1.0 \times 10^7$

and Prandtl number $Pr = 0.7$ is analysed with the Kolmogorov and Yaglom equations (Kolmogorov 1941*a*; Yaglom 1949) extended to an inhomogeneous and anisotropic flow (Hill 2002; Marati, Casciola & Piva 2004; Burattini, Antonia & Danaila 2005; Valente & Vassilicos 2015). These are the evolution equations for the second-order velocity and temperature structure functions, which can be exactly derived from the governing equations and allow for a neat description of the turbulent processes occurring at different scales and locations in physical space. Two characteristic scales are identified using these budgets, one for the velocity field, ℓ_c^u, and one for the temperature field, ℓ_c^θ, which depend on the wall distance and separate the large inhomogeneous scales from the small dissipative ones.

In the LES framework, the relative position of the filter length, ℓ_F, with respect to ℓ_c^u and ℓ_c^θ determines up to what extent the flow dynamics is going to be captured and what should be reproduced by the SGS model. In particular, for filter lengths smaller than the identified cross-over scales, the most inhomogeneous and energetic features of the flow are arguably captured and the purely dissipative role of the subgrid scales can be reproduced by means of simple and rather universal closures. In the second part of this work, the effect of the filter length on the resolved and subgrid dynamics is rigorously assessed. For this purpose, the velocity and the scalar fields obtained from a DNS are split into resolved and subgrid components using a spectral cutoff filter and analysed by means of filtered single-point and two-point budgets. While the filtered Kolmogorov equation has already been employed by Cimarelli & De Angelis (2011), the filtered Yaglom equation is presented and discussed here for the first time.

The paper is organized as follows. The theoretical framework consisting of single-point and scale-by-scale budgets is presented in § 2. The fully resolved dynamics of RBC is then discussed in § 3, followed by the analysis of the filtered dataset in § 4. A summary of the main findings and some concluding remarks are made in § 5.

2. The Kolmogorov and Yaglom equations

In the framework of homogeneous and isotropic turbulence transporting a passive temperature, the Kolmogorov–Obukhov–Corrsin (K41-OC) theory states that, at sufficiently high Reynolds numbers, a range of scales exists where turbulent kinetic energy and temperature variance are only transferred from large to small scales (Kolmogorov 1941*b*; Corrsin 1951; Obukhov 1968). This exact and non-trivial result can be derived from the equations for the second-order velocity and temperature structure functions $\langle \delta u^2 \rangle = \langle \delta u_i \delta u_i \rangle$ and $\langle \delta \theta^2 \rangle = \langle \delta \theta \delta \theta \rangle$. Here the angular brackets $\langle \cdot \rangle$ denote the spatial average along the homogeneous directions, and the ensemble average over different configurations, $\delta u_i = u_i(x_j + r_j/2) - u_i(x_j - r_j/2)$ and $\delta \theta = \theta(x_j + r_j/2) - \theta(x_j - r_j/2)$ are the fluctuating velocity and temperature increments between the points $x_j + r_j/2$ and $x_j - r_j/2$, and the indices $i, j = 1, 2, 3$ denote the Cartesian components.

Following the heuristic approach proposed by Davidson, Pearson & Staplehurst (2004), the second-order structure functions $\langle \delta u^2 \rangle$ and $\langle \delta \theta^2 \rangle$ can be interpreted as the turbulent kinetic energy and the temperature variance, respectively, contained by the eddies of length scale smaller than $r = \sqrt{r_i r_i}$. Indeed, turbulent scales less than r can actively modulate the signal at $x_j + r_j/2$ or $x_j - r_j/2$ but not at both locations simultaneously; thus, they contribute significantly to the structure function. On the other hand, eddies of size much larger than r tend to induce similar signals at both points, with consequent little contribution to the fluctuating increment. In summary, the structure function can be considered along the same line as a high-pass filter,

capable of retaining the fluctuations at scales smaller than the filter length r and of damping the information from eddies of size larger than r. Hence, together with the turbulent spectrum, it can be used to study the multiscale features of turbulence (see e.g. Dupuy, Toutant & Bataille 2018). In view of this, throughout this paper we will refer to $\langle \delta u^2 \rangle$ and $\langle \delta \theta^2 \rangle$ also as scale energy and scale variance, respectively, adopting the nomenclature introduced by Danaila *et al.* (2001) and employed later by Marati *et al.* (2004), Cimarelli & De Angelis (2011), Cimarelli, De Angelis & Casciola (2013) and Togni, Cimarelli & De Angelis (2015).

In general, the second-order structure function depends both on the separation vector r_j and on the spatial location of the midpoint x_j. However, in the case of homogeneous turbulence, the dependence of the scale energy and the scale variance on the midpoint x_j drops and, starting from the governing equations, it is possible to derive the following exact equations for $\langle \delta u^2 \rangle$ and $\langle \delta \theta^2 \rangle$:

$$-\frac{\partial \langle \delta u^2 \delta u_i \rangle}{\partial r_i} + 2\langle \delta f_i^u \delta u_i \rangle + 2\nu \frac{\partial^2 \langle \delta u^2 \rangle}{\partial r_j \partial r_j} - 4\langle \epsilon \rangle = 0, \tag{2.1}$$

$$-\frac{\partial \langle \delta \theta^2 \delta u_i \rangle}{\partial r_i} + 2\langle \delta f_i^\theta \delta u_i \rangle + 2\kappa \frac{\partial^2 \langle \delta \theta^2 \rangle}{\partial r_j \partial r_j} - 2\langle \chi \rangle = 0, \tag{2.2}$$

where ν is the kinematic viscosity, κ is the thermal diffusivity, $\epsilon = 2\nu(S_{ij}S_{ij})$ is the dissipation of turbulent kinetic energy, $S_{ij} = 0.5(\partial u_i/\partial x_j + \partial u_j/\partial x_i)$ is the fluctuating strain-rate tensor, $\chi = 2\kappa(\partial\theta/\partial x_i)(\partial\theta/\partial x_i)$ is the dissipation of temperature variance, and $2\langle \delta f_i^u \delta u_i \rangle$ and $2\langle \delta f_i^\theta \delta u_i \rangle$ are the homogeneous source terms due to the external forcing f_i^u and f_i^θ active at large scales. The first term in (2.1) and (2.2) denotes the rate at which scales smaller than r receive (release) turbulent kinetic energy and temperature variance from (to) larger ones via inertial mechanisms, whereas the third term in (2.1) and (2.2) is indicative of the amount of turbulent kinetic energy and temperature variance diffused in the space of scales. In the case of high-intensity turbulent flows, an inertial range is supposed to develop for $\eta_k, \eta_b \ll r \ll \ell_0$, where η_k, η_b and ℓ_0 are the Kolmogorov, the Batchelor and the integral scales, respectively. Both production and viscous diffusion effects are negligible within this range, thus (2.1) and (2.2) reduce to

$$\frac{\partial \langle \delta u^2 \delta u_i \rangle}{\partial r_i} = -4\langle \epsilon \rangle, \tag{2.3}$$

$$\frac{\partial \langle \delta \theta^2 \delta u_i \rangle}{\partial r_i} = -2\langle \chi \rangle, \tag{2.4}$$

stating that the amount of turbulent kinetic energy and temperature variance transferred per unit time to scales less than r is equal to the average dissipation rates. It should be pointed out that (2.3) and (2.4) further simplify to the familiar four-fifths and four-thirds laws, respectively, if turbulence is assumed to be also isotropic.

The fundamental aspect of actual turbulent flows is the presence of a cycle along which fluctuations are generated, transported among different scales and space locations, and finally dissipated. Inhomogeneity modifies the scale-by-scale budgets (2.1) and (2.2) by introducing an autonomous production, a transport in physical space and by spatially modulating the balances. Fully developed turbulence in laterally unbounded RBC is statistically inhomogeneous in the wall-normal direction but homogeneous and isotropic in the wall-parallel planes. We exploit these symmetries,

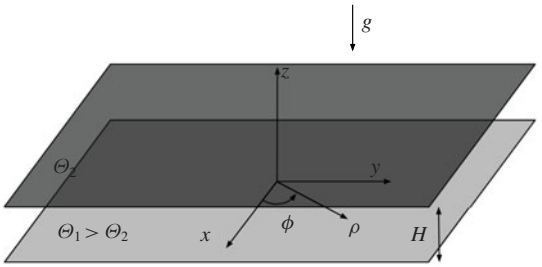

FIGURE 1. Sketch of the Rayleigh–Bénard convection set-up.

and in particular the isotropy in the wall-parallel planes, by considering a cylindrical coordinate system (ρ, ϕ, z) rather than a Cartesian one (x, y, z); see the sketch in figure 1. The wall-parallel coordinates are $x = x_1$ and $y = x_2$ while the wall-normal coordinate, $z = x_3$, is zero at the lower wall. The cylindrical coordinates are defined such that $\rho = \sqrt{x^2 + y^2}$ and $\phi = \arctan(y/x)$. The scale-by-scale budgets for RBC can be derived starting from the continuity, momentum and energy equations under the Boussinesq approximation (Hill 2002) and, for a cylindrical coordinate system, result in

$$-\frac{\partial\langle w^\dagger \delta u^2\rangle}{\partial z} - 2\frac{\partial\langle \delta p \delta w\rangle}{\partial z} + \frac{\nu}{2}\frac{\partial^2\langle \delta u^2\rangle}{\partial z^2} - \frac{1}{r_\rho}\frac{\partial}{\partial r_\rho}(r_\rho\langle \delta u^2 \delta u_\rho\rangle)$$
$$-\frac{\partial\langle \delta u^2 \delta w\rangle}{\partial r_z} + 2\alpha g\langle \delta\theta\delta w\rangle + \frac{2\nu}{r_\rho}\frac{\partial}{\partial r_\rho}\left(r_\rho\frac{\partial\langle \delta u^2\rangle}{\partial r_\rho}\right) + 2\nu\frac{\partial^2\langle \delta u^2\rangle}{\partial r_z^2} - 4\langle\tilde{\epsilon}^\dagger\rangle = 0 \quad (2.5)$$

and

$$-\frac{\partial\langle w^\dagger \delta\theta^2\rangle}{\partial z} + \frac{\kappa}{2}\frac{\partial^2\langle \delta\theta^2\rangle}{\partial z^2} - \frac{1}{r_\rho}\frac{\partial}{\partial r_\rho}(r_\rho\langle \delta\theta^2 \delta u_\rho\rangle) - \frac{\partial\langle \delta\theta^2\delta w\rangle}{\partial r_z}$$
$$-2\langle w^\dagger\delta\theta\rangle\frac{\partial\delta\Theta}{\partial z} - 2\langle\delta w\delta\theta\rangle\left(\frac{\mathrm{d}\Theta}{\mathrm{d}z}\right)^\dagger + \frac{2\kappa}{r_\rho}\frac{\partial}{\partial r_\rho}\left(r_\rho\frac{\partial\langle\delta\theta^2\rangle}{\partial r_\rho}\right) + 2\kappa\frac{\partial^2\langle\delta\theta^2\rangle}{\partial r_z^2}$$
$$-2\langle\chi^\dagger\rangle = 0, \quad (2.6)$$

where g is the gravity acceleration, α is the thermal expansion coefficient and $\tilde{\epsilon} = \nu(\partial u_i/\partial x_j)(\partial u_i/\partial x_j)$ is the pseudo-dissipation of turbulent kinetic energy. The dagger $\dagger$ denotes the midpoint average, $\beta^\dagger = (\beta(x_j - r_j/2) + \beta(x_j + r_j/2))/2$ for the generic quantity β. The radial, the circumferential and the vertical components of the separation vector are r_ρ, r_ϕ and r_z, whereas the same components of the velocity structure function are δu_ρ, δu_ϕ and δw. Let us note that all the r_ϕ-derivative terms arising from the formulation in cylindrical coordinates are zero for statistical isotropy while, for statistical homogeneity, also the ϕ- and ρ-derivatives are null.

An additional class of terms, namely the ones with the z-derivative, appear in the inhomogeneous case, denoting the amount of scale energy and scale variance received (released) from (to) other wall distances. Moreover, $2\alpha g\langle\delta\theta\delta w\rangle$ and $-2\langle w^\dagger\delta\theta\rangle(\partial\delta\Theta/\partial z) - 2\langle\delta w\delta\theta\rangle(\mathrm{d}\Theta/\mathrm{d}z)^\dagger$ are the inhomogeneous production terms, where Θ is the mean temperature. At sufficiently high Reynolds numbers, an inertial range of scales is assumed to exist in which turbulence is locally homogeneous and isotropic, viscous effects are negligible, and temperature acts as a passive scalar

(Lohse & Xia 2010). In this case, it is easy to demonstrate that (2.5) and (2.6) simplify to (2.3) and (2.4) and, with further manipulations, to the four-fifths and four-thirds laws, respectively.

Equations (2.5) and (2.6), written in the complete three-dimensional (r_ρ, r_z, z) space, are the Kolmogorov and Yaglom equations for RBC. The Kolmogorov equation for an axisymmetric flow has already been proposed by Danaila *et al.* (2012), while the Yaglom equation has been extended before only to homogeneous anisotropic turbulence (Gauding *et al.* 2014). For the sake of simplicity, we restrict the following analysis to the reduced (r_ρ, z) space, where $r_z = 0$ (Cimarelli *et al.* 2016). The reduced scale-by-scale budgets are non-dimensionalized using H, $\Delta\Theta = \Theta_1 - \Theta_2$ and $U_f = \sqrt{g\alpha\Delta\Theta H}$ as characteristic length, temperature and velocity scales, where H is the height of the fluid layer, Θ_1 and Θ_2 are the temperature of the lower and upper walls, respectively, and U_f is the free-fall velocity. The resulting equations, hereafter referred to as reduced Kolmogorov and Yaglom equations, can be written in a compact form, i.e.

$$T_c^u + I_r^u + \Pi^u + E_e^u = 0, \tag{2.7}$$

$$T_c^\theta + I_r^\theta + \Pi^\theta + E_e^\theta = 0, \tag{2.8}$$

where $T_c^u = I_c^u + P + D_c^u$ and $T_c^\theta = I_c^\theta + D_c^\theta$ represent the sum of the transport terms in physical space and hence will be hereafter called the overall transports. On the other hand, $E_e^u = D_r^u + E^u$ and $E_e^\theta = D_r^\theta + E^\theta$ represent the overall effect of viscosity on transporting scale energy and scale variance to the smallest scales of the flow by D_r^u and D_r^θ, where they are finally dissipated by E^u and E^θ. Accordingly, E_e^u and E_e^θ will be hereafter called effective dissipations. The different contributions to the overall transports and to the effective dissipations are, in order,

$$\left.\begin{aligned} I_c^u &= -\frac{\partial\langle w^\dagger \delta u^2\rangle}{\partial z}, \quad P = -2\frac{\partial\langle \delta p \delta w\rangle}{\partial z}, \quad D_c^u = \frac{1}{2}\sqrt{\frac{Pr}{Ra}}\frac{\partial^2\langle\delta u^2\rangle}{\partial z^2}, \\ I_c^\theta &= -\frac{\partial\langle w^\dagger \delta\theta^2\rangle}{\partial z}, \quad D_c^\theta = \frac{1}{2\sqrt{PrRa}}\frac{\partial^2\langle\delta\theta^2\rangle}{\partial z^2}, \end{aligned}\right\} \tag{2.9}$$

and

$$\left.\begin{aligned} D_r^u &= 2\sqrt{\frac{Pr}{Ra}}\frac{1}{r_\rho}\frac{\partial}{\partial r_\rho}\left(r_\rho\frac{\partial\langle\delta u^2\rangle}{\partial r_\rho}\right) + 2\sqrt{\frac{Pr}{Ra}}\frac{\partial^2\langle\delta u^2\rangle}{\partial r_z^2}\bigg|_{r_z=0}, \quad E^u = -4\langle\tilde{\epsilon}\rangle, \\ D_r^\theta &= \frac{2}{\sqrt{PrRa}}\frac{1}{r_\rho}\frac{\partial}{\partial r_\rho}\left(r_\rho\frac{\partial\langle\delta\theta^2\rangle}{\partial r_\rho}\right) + \frac{2}{\sqrt{PrRa}}\frac{\partial^2\langle\delta\theta^2\rangle}{\partial r_z^2}\bigg|_{r_z=0}, \quad E^\theta = -2\langle\chi\rangle, \end{aligned}\right\} \tag{2.10}$$

while the transports in the space of scales and the production terms are

$$\left.\begin{aligned} I_r^u &= -\frac{1}{r_\rho}\frac{\partial}{\partial r_\rho}(r_\rho\langle\delta u^2\delta u_\rho\rangle) - \frac{\partial\langle\delta u^2\delta w\rangle}{\partial r_z}\bigg|_{r_z=0}, \quad \Pi^u = 2\langle\delta\theta\delta w\rangle, \\ I_r^\theta &= -\frac{1}{r_\rho}\frac{\partial}{\partial r_\rho}(r_\rho\langle\delta\theta^2\delta u_\rho\rangle) - \frac{\partial\langle\delta\theta^2\delta w\rangle}{\partial r_z}\bigg|_{r_z=0}, \quad \Pi^\theta = -2\langle\delta w\delta\theta\rangle\frac{\mathrm{d}\Theta}{\mathrm{d}z}. \end{aligned}\right\} \tag{2.11}$$

It must be pointed out that the contribution of the term $-2\langle w^\dagger\delta\theta\rangle(\partial\delta\Theta/\partial z)$ to the production of scale variance vanishes, since $\delta\Theta = 0$ for $r_z = 0$. Finally, the

non-dimensional groups appearing are the Rayleigh number, $Ra = g\alpha\Delta\Theta H^3/\nu\kappa$, and the Prandtl number, $Pr = \nu/\kappa$.

Let us extend the Kolmogorov and Yaglom equations to filtered velocity and temperature fields. Starting from the filtered continuity, momentum and energy equations under the Boussinesq approximation and by following the same procedure used to derive (2.5) and (2.6) (Hill 2002), it is possible to obtain the budgets of resolved scale energy $\langle\delta\bar{u}^2\rangle = \langle\delta\bar{u}_i\delta\bar{u}_i\rangle$ and resolved scale variance $\langle\delta\bar{\theta}^2\rangle = \langle\delta\bar{\theta}\delta\bar{\theta}\rangle$:

$$
\begin{aligned}
&-\frac{\partial\langle\bar{w}^\dagger\delta\bar{u}^2\rangle}{\partial z} - 2\frac{\partial\langle\delta\bar{p}\delta\bar{w}\rangle}{\partial z} + \frac{\nu}{2}\frac{\partial^2\langle\delta\bar{u}^2\rangle}{\partial z^2} - \frac{1}{r_\rho}\frac{\partial}{\partial r_\rho}(r_\rho\langle\delta\bar{u}^2\delta\bar{u}_\rho\rangle)\\
&\quad - \frac{\partial\langle\delta\bar{u}^2\delta\bar{w}\rangle}{\partial r_z} + 2\alpha g\langle\delta\bar{\theta}\delta\bar{w}\rangle + \frac{2\nu}{r_\rho}\frac{\partial}{\partial r_\rho}\left(r_\rho\frac{\partial\langle\delta\bar{u}^2\rangle}{\partial r_\rho}\right) + 2\nu\frac{\partial^2\langle\delta\bar{u}^2\rangle}{\partial r_z^2} - 4\langle\bar{\tilde{\epsilon}}^\dagger\rangle\\
&\quad - \frac{\partial\langle\delta\tau_{i3}\delta\bar{u}_i\rangle}{\partial z} - \frac{4}{r_\rho}\frac{\partial}{\partial r_\rho}(r_\rho\langle\tau_{ij}^\dagger\delta\bar{u}_i\hat{\rho}_j\rangle) - 4\frac{\partial\langle\tau_{i3}^\dagger\delta\bar{u}_i\rangle}{\partial r_z}\bigg|_{r_z=0} - 4\langle\epsilon_{sgs}\rangle = 0
\end{aligned}
\tag{2.12}
$$

and

$$
\begin{aligned}
&-\frac{\partial\langle\bar{w}^\dagger\delta\bar{\theta}^2\rangle}{\partial z} + \frac{\kappa}{2}\frac{\partial^2\langle\delta\bar{\theta}^2\rangle}{\partial z^2} - \frac{1}{r_\rho}\frac{\partial}{\partial r_\rho}(r_\rho\langle\delta\bar{\theta}^2\delta\bar{u}_\rho\rangle) - \frac{\partial\langle\delta\bar{\theta}^2\delta\bar{w}\rangle}{\partial r_z}\\
&\quad - 2\langle\bar{w}^\dagger\delta\bar{\theta}\rangle\frac{\partial\delta\bar{\Theta}}{\partial z} - 2\langle\delta\bar{w}\delta\bar{\theta}\rangle\left(\frac{\mathrm{d}\bar{\Theta}}{\mathrm{d}z}\right)^\dagger + \frac{2\kappa}{r_\rho}\frac{\partial}{\partial r_\rho}\left(r_\rho\frac{\partial\langle\delta\bar{\theta}^2\rangle}{\partial r_\rho}\right) + 2\kappa\frac{\partial^2\langle\delta\bar{\theta}^2\rangle}{\partial r_z^2}\\
&\quad - 2\langle\bar{\chi}^\dagger\rangle - \frac{\partial\langle\delta q_z\delta\bar{\theta}\rangle}{\partial z} - \frac{4}{r_\rho}\frac{\partial}{\partial r_\rho}(r_\rho\langle q_\rho^\dagger\delta\bar{\theta}\rangle) - 4\frac{\partial\langle q_z^\dagger\delta\bar{\theta}\rangle}{\partial r_z}\bigg|_{r_z=0} - 2\langle\chi_{sgs}\rangle = 0.
\end{aligned}
\tag{2.13}
$$

Equations (2.12) and (2.13) share several types of terms with the corresponding unfiltered equations (2.5) and (2.6) which can be better highlighted by considering the filtered reduced Kolmogorov and Yaglom equations,

$$\bar{T}_c^u + \bar{I}_r^u + \bar{\Pi}^u + \bar{E}_e^u + T_{c,sgs}^u + T_{r,sgs}^u + E_{sgs}^u = 0, \tag{2.14}$$

$$\bar{T}_c^\theta + \bar{I}_r^\theta + \bar{\Pi}^\theta + \bar{E}_e^\theta + T_{c,sgs}^\theta + T_{r,sgs}^\theta + E_{sgs}^\theta = 0, \tag{2.15}$$

where it is possible to recognize that the first four terms in (2.14) and (2.15) are the same terms composing the unfiltered reduced budgets (2.7) and (2.8), with the difference that they are constituted by the filtered velocity, temperature and pressure fields. Indeed, the completely new terms in the filtered budgets are entirely due to subgrid-scale effects, i.e.

$$
\left.
\begin{aligned}
T_{c,sgs}^u &= -\frac{\partial\langle\delta\tau_{i3}\delta\bar{u}_i\rangle}{\partial z}, \quad T_{r,sgs}^u = -\frac{4}{r_\rho}\frac{\partial}{\partial r_\rho}(r_\rho\langle\tau_{ij}^\dagger\delta\bar{u}_i\hat{\rho}_j\rangle) - 4\frac{\partial\langle\tau_{i3}^\dagger\delta\bar{u}_i\rangle}{\partial r_z}\bigg|_{r_z=0},\\
&\qquad E_{sgs}^u = -4\langle\epsilon_{sgs}\rangle,\\
T_{c,sgs}^\theta &= -\frac{\partial\langle\delta q_z\delta\bar{\theta}\rangle}{\partial z}, \quad T_{r,sgs}^\theta = -\frac{4}{r_\rho}\frac{\partial}{\partial r_\rho}(r_\rho\langle q_\rho^\dagger\delta\bar{\theta}\rangle) - 4\frac{\partial\langle q_z^\dagger\delta\bar{\theta}\rangle}{\partial r_z}\bigg|_{r_z=0},\\
&\qquad E_{sgs}^\theta = -2\langle\chi_{sgs}\rangle,
\end{aligned}
\right\}
\tag{2.16}
$$

and represent the transport in physical space, the transport in the space of scales and the dissipation of resolved scale energy and resolved scale variance due to the

fluctuating SGS stress tensor, $\tau_{ij} = \overline{u_i u_j} - \bar{u}_i \bar{u}_j$, and the fluctuating SGS heat flux, $q_i = \overline{u_i \theta} - \bar{u}_i \bar{\theta}$. Here, q_ρ and q_z are the radial and vertical components of the SGS heat flux, $\hat{\rho}_j$ is the radial unit vector, $\bar{\tilde{\epsilon}} = \sqrt{Pr/Ra}(\partial \bar{u}_i/\partial x_j)(\partial \bar{u}_i/\partial x_j)$ is the pseudo-dissipation of resolved turbulent kinetic energy, and $\bar{\chi} = 2(PrRa)^{-1/2}(\partial \bar{\theta}/\partial x_i)(\partial \bar{\theta}/\partial x_i)$ is the dissipation of resolved temperature variance. The subgrid dissipations are $\epsilon_{sgs} = -\tau_{ij}\bar{S}_{ij}$ and $\chi_{sgs} = -2q_i\bar{Q}_i$, where $\bar{S}_{ij} = 0.5(\partial \bar{u}_i/\partial x_j + \partial \bar{u}_j/\partial x_i)$ is the resolved fluctuating strain-rate tensor and $\bar{Q}_i = \partial \bar{\theta}/\partial x_i$ is the gradient of the resolved fluctuating temperature.

Let us point out that the filtered reduced Kolmogorov equation (2.14) has already been employed for the *a priori* (Cimarelli & De Angelis 2012) and the *a posteriori* (Cimarelli & De Angelis 2014) testing of some SGS models for the turbulent channel flow, proving to be a precious framework for the assessment of the dynamics induced by τ_{ij}. The filtered reduced Yaglom equation (2.15), on the other hand, is presented here for the first time.

Equations (2.7), (2.8) and (2.14), (2.15) manifest a well-defined asymptotic behaviour as larger separations are approached. For $r_\rho \gg \ell$, where ℓ is the relevant correlation length, quantities evaluated at $(\rho + r_\rho/2, \phi, z)$ and $(\rho - r_\rho/2, \phi, z)$ become uncorrelated and (2.7), (2.8) reduce, within a factor of four and two, respectively, to the budgets of turbulent kinetic energy $\langle k \rangle = 0.5\langle u_i u_i \rangle$ and temperature variance $\langle \theta^2 \rangle$,

$$4(t_c^u + \pi^u - \langle \tilde{\epsilon} \rangle) = 0, \tag{2.17}$$

$$2(t_c^\theta + \pi^\theta - \langle \chi \rangle) = 0, \tag{2.18}$$

where

$$t_c^u = -\frac{\mathrm{d}\langle kw \rangle}{\mathrm{d}z} - \frac{\mathrm{d}\langle wp \rangle}{\mathrm{d}z} + \sqrt{\frac{Pr}{Ra}}\frac{\mathrm{d}^2\langle k \rangle}{\mathrm{d}z^2}, \quad \pi^u = \langle w\theta \rangle, \tag{2.19}$$

$$t_c^\theta = -\frac{\mathrm{d}\langle \theta^2 w \rangle}{\mathrm{d}z} + \frac{1}{\sqrt{PrRa}}\frac{\mathrm{d}^2\langle \theta^2 \rangle}{\mathrm{d}z^2}, \quad \pi^\theta = -2\langle w\theta \rangle \frac{\mathrm{d}\Theta}{\mathrm{d}z}, \tag{2.20}$$

are the overall transports and the productions of $\langle k \rangle$ and $\langle \theta^2 \rangle$. Analogously, the filtered reduced Kolmogorov and Yaglom equations converge respectively to four times the budget of resolved turbulent kinetic energy $\bar{k} = 0.5(\bar{u}_i \bar{u}_i)$ and two times the budget of resolved temperature variance $\langle \bar{\theta}^2 \rangle$,

$$4(\bar{t}_c^u + \bar{\pi}^u - \langle \bar{\tilde{\epsilon}} \rangle + t_{c,sgs}^u - \langle \epsilon_{sgs} \rangle) = 0, \tag{2.21}$$

$$2(\bar{t}_c^\theta + \bar{\pi}^\theta - \langle \bar{\chi} \rangle + t_{c,sgs}^\theta - \langle \chi_{sgs} \rangle) = 0, \tag{2.22}$$

where the terms under the overbar and the corresponding ones without it are identical except that they consider filtered quantities. Finally, the SGS transports of $\langle \bar{k} \rangle$ and $\langle \bar{\theta}^2 \rangle$ are

$$t_{c,sgs}^u = -\frac{\mathrm{d}\langle \tau_{i3}\bar{u}_i \rangle}{\mathrm{d}z} \quad \text{and} \quad t_{c,sgs}^\theta = -2\frac{\mathrm{d}\langle q_z \bar{\theta} \rangle}{\mathrm{d}z}. \tag{2.23a,b}$$

It is well known that the thermal boundary layer thickness represents a characteristic length scale in turbulent RBC. As a result of that, in what follows, we analyse all the budgets presented up to now as a function of spatial variables that are non-dimensionalized with respect to H/Nu instead of H, where Nu is the Nusselt number, and we denote them with the superscript *. The choice of the length scale

H/Nu, which is twice the commonly defined thermal boundary layer thickness, allows for a more appropriate comparison of the results when different Rayleigh numbers are considered. In particular, as shown in Togni *et al.* (2015), by normalizing the independent variables with H/Nu, the shape of the temperature statistics becomes Ra-invariant, whereas the velocity statistics exhibit a rather small drift in the profile shape.

3. Study of the unfiltered dataset

The reduced Kolmogorov and Yaglom equations, equations (2.7) and (2.8), respectively, represent two useful tools for investigating the self-sustained mechanisms of convective turbulence at different scales and locations in physical space. The essential features of the multiscale analysis are reported in this section, drawing attention to their relevance in the LES framework. A thorough description of the budgets is beyond the purpose of this work; hence, we would like to point the reader to Togni *et al.* (2015) for further details. See also Antonia & Orlandi (2003) for additional information on the temperature structure function scaling at different Schmidt numbers.

Each term of (2.7) and (2.8) is computed using a DNS dataset of turbulent RBC at $Ra = 1.0 \times 10^7$ and $Pr = 0.7$. The numerical simulation solves the continuity, momentum and energy equations under the Boussinesq approximation using a pseudospectral method that discretizes the space with Chebyshev polynomials in the wall-normal direction and with Fourier modes in the wall-parallel ones. Time integration is performed with a fourth-order Runge–Kutta scheme for the nonlinear terms and a second-order-accurate Crank–Nicolson scheme for the linear ones. The dimensions of the numerical box are $8 \times 8 \times 1$ along x, y, z, where periodic boundary conditions are imposed at the lateral sidewalls and isothermal/no-slip boundary conditions are used on the top and bottom plates. The DNS approach requires the number of fully dealiased modes (N_x, N_y) and polynomials (N_z) to be sufficiently high to resolve all the degrees of freedom of the system. The present simulation is performed with $N_x \times N_y \times N_z = 540 \times 540 \times 257$ and, as shown in Togni *et al.* (2015), where the details of the present simulation are reported, *a posteriori* tests prove that this resolution is sufficient to capture the smallest scale of the flow. Regarding the temporal advancement, an adaptive time step is set to ensure a Courant–Friedrichs–Lewy number below 2.5. For the sake of statistical convergence, after the initial transient of the flow, the DNS is run for a time period $T = 250$, which corresponds to 125 times the large-eddy turnover time $2H/U_f = 2$, and the fields are stored every $\Delta\tau = 5$ in order to collect samples that are likely to be uncorrelated. An estimate of the statistical convergence of the data is given by the accuracy with which the Kolmogorov and Yaglom equations are satisfied; see the circles shown in figure 3.

Before presenting the scale-by-scale results, let us report a brief description of the flow dynamics in terms of the single-point budgets of turbulent kinetic energy and temperature variance; see equations (2.17) and (2.18), respectively. According to this analysis, the domain can be split into three fundamental parts: a bulk region for $0.8 \lesssim z^* < 7.8$ (where $z^* = Nu/2 = 7.8$ corresponds to the centre of the cell), a transitional layer for $0.2 \lesssim z^* \lesssim 0.8$ and a viscous layer for $z^* \lesssim 0.2$; see figure 2(*a*,*b*). The buoyant production of turbulent kinetic energy overcomes the viscous dissipation inside the bulk region and the resulting excess of energy is mostly transported towards the wall by means of pressure mechanisms. The transitional region, located between the bulk

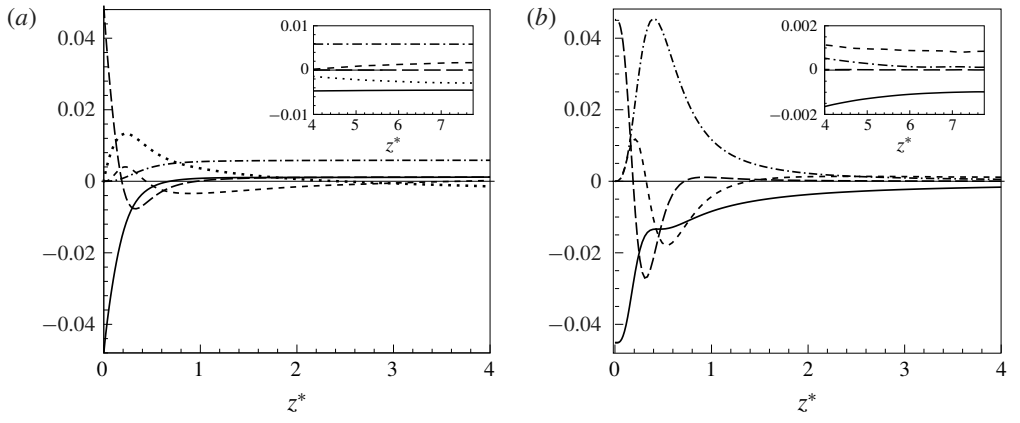

FIGURE 2. (*a*) Terms of the turbulent kinetic energy budget (2.17) as a function of z^*: inertial transport (dashed line), pressure transport (dotted line), viscous transport (long dashed line), production (dot-dashed line) and dissipation (solid line). (*b*) Terms of the temperature variance budget (2.18) as a function of z^*: inertial transport (dashed line), viscous transport (long dashed line), production (dot-dashed line) and dissipation (solid line).

and the viscous layer, is sustained by the inviscid transport coming from the core rather than by the local production; from there, energy diffuses into the viscous layer where it balances the local dissipation rate. Regarding the budget for the temperature variance, the transitional layer is a source region that irradiates thermal fluctuations towards the bulk and towards the viscous layer by means of inertial and viscous mechanisms. The bulk region and the viscous layer are, on the other hand, two sink regions for thermal fluctuations, as they mostly receive and dissipate the temperature variance that is generated inside the transitional layer. See Togni *et al.* (2015) for a detailed discussion of the turbulent kinetic energy and temperature variance budgets.

The mechanisms of production, transport and dissipation of turbulent fluctuations are inherently multiscale; therefore, they depend not only on the location in physical space but also on the length scale considered. The reduced Kolmogorov and Yaglom equations partially describe this complex phenomenology by addressing the dynamics at separations in the horizontal planes (i.e. for $r_z^* = 0$), and at different wall distances z^*. Here, to avoid the complexity that a detailed investigation would imply, we only evaluate the Kolmogorov and Yaglom equations at two relevant distances from the wall, $z^* = 6$ and $z^* = 0.5$, as representative of the typical scale-by-scale behaviours in the bulk region and transitional layer, respectively.

Let us first consider the bulk region. As shown in figure 3(*a*), the examination of the reduced Kolmogorov equation from large to small r_ρ^* reveals a range of separations where the production Π^u is important ($r_\rho^* \gtrsim 3$), followed by a range dominated by a positive inertial transfer, $I_r^u > 0$ ($1 \lesssim r_\rho^* \lesssim 3$). Inside the inertia-dominated range, scales smaller than those separations receive energy from larger ones via a direct cascade rather than produce it by themselves. At even smaller separations ($r_\rho^* \lesssim 1$), D_r^u increases up to E^u, which means that eddies of size less than r_ρ^* start to be affected by viscous mechanisms and to dissipate the energy cascading from larger ones.

It is worth noting that both the production Π^u and the overall transport T_c^u reach a well-defined maximum around $r_\rho^* = 40$, meaning that turbulent kinetic energy is

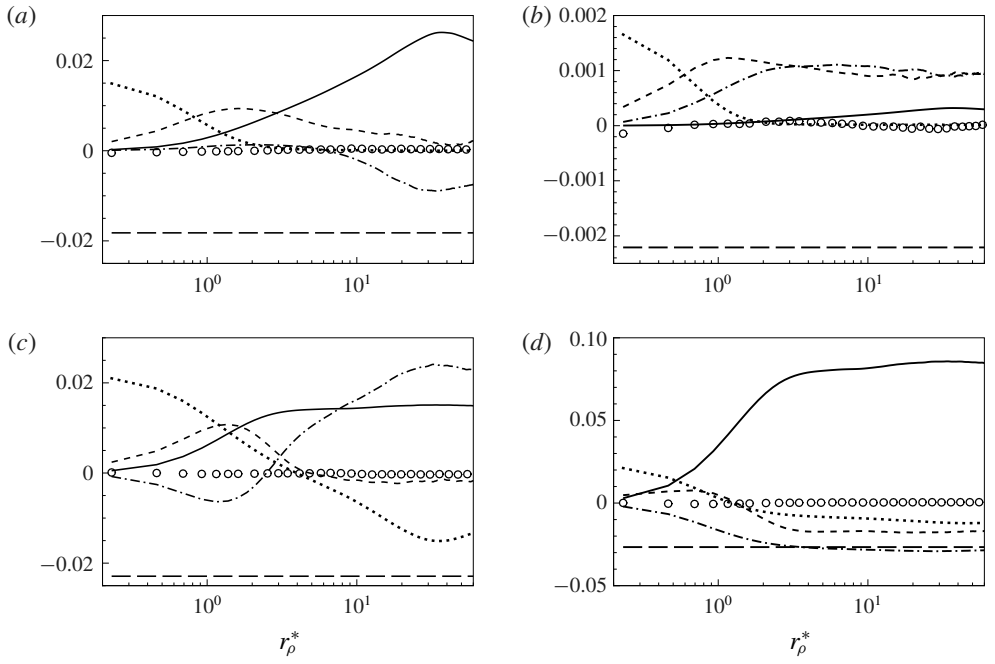

FIGURE 3. Scale-by-scale budgets (*a*,*c*) of $\langle \delta u^2 \rangle$ and (*b*,*d*) of $\langle \delta\theta^2 \rangle$ as functions of r_ρ^* inside (*a*,*b*) the bulk region at $z^* = 6$ and inside (*c*,*d*) the transitional layer at $z^* = 0.5$. Curves: Π^u and Π^θ (solid line), T_c^u and T_c^θ (dot-dashed line), I_r^u and I_r^θ (dashed line), D_r^u and D_r^θ (dotted line), E^u and E^θ (long-dashed line), and $T_c^u + I_r^u + D_r^u + \Pi^u + E^u$ and $T_c^\theta + I_r^\theta + D_r^\theta + \Pi^\theta + E^\theta$ (circles). The maximum separation $r_\rho^* = 60 \approx 4Nu$ is limited by periodicity along x and y.

essentially produced and transported by eddies smaller than this characteristic length. Such an intriguing behaviour can be further investigated by expanding the production term as follows:

$$\Pi^u(r_\rho, z) = \Pi_I^u(z) - \Pi_{II}^u(r_\rho, z), \tag{3.1}$$

where

$$\Pi_I^u = 4\langle \theta w \rangle \quad \text{and} \quad \Pi_{II}^u = 4\langle \theta(\rho + r_\rho/2, \phi, z) w(\rho - r_\rho/2, \phi, z) \rangle \tag{3.2a,b}$$

are, in order, four times the production of turbulent kinetic energy and four times the two-point cross-correlation between vertical velocity and temperature fluctuation. It is evident that, for every wall distance, the maximum of Π^u occurs at the separation which maximizes $-\Pi_{II}^u$ or, in other words, at the distance where w and θ are maximally anticorrelated. Hence, the characteristic length $r_\rho^* = 40$ seems to be strictly connected with the flow topology, as it represents a measure of the average distance between warm fluid moving upwards and cold fluid moving downwards. Evidence of large-scale circulations, namely clusters of ascending warm and descending cold plumes, has been reported also in the absence of a lateral confinement and these structures show a lateral size that is around two times the height of the domain, i.e. comparable with the location of the maximum around $r_\rho^* = 40$ (Van Reeuwijk, Jonker & Hanjalić 2005).

The terms of the reduced Yaglom equation are represented in figure 3(*b*) for the same location in the bulk. In this case, the production Π^θ is negligible in comparison with the overall transport T_c^θ at every separation; however, a range dominated by the term T_c^θ due to the spatial inhomogeneity ($r_\rho^* \gtrsim 3$), followed by a direct cascade ($0.5 \lesssim r_\rho^* \lesssim 3$) and closed by dissipation ($r_\rho^* \lesssim 0.5$) can be identified as in figure 3(*a*). Here, it is worth noting that the overall transport in physical space does not exhibit an evident peak like in the reduced Kolmogorov equation; thus, a characteristic length of the inhomogeneous processes cannot be equally identified.

A completely different scenario occurs inside the transitional layer. As shown in figure 3(*c*), the analysis of the reduced Kolmogorov equation at $z^* = 0.5$ reveals that a production-dominated range, followed by an inertial direct cascade, is no longer recognizable. Indeed, both the production and the transport in physical space are important throughout the entire range of separations, while the viscous dissipation is not restricted only to the small scales but substantially affects also the larger ones, as can be seen from the well-defined peak of D_r^u at $r_\rho^* \approx 35$. For $r_\rho^* \gtrsim 5$, the net amount of energy produced and transported at scales less than r_ρ^* cannot be entirely dissipated at this wall distance, i.e. $\Pi^u + T_c^u > -E_e^u$; hence velocity fluctuations start to flow towards larger scales in a reverse cascade process, $I_r^u < 0$, to be finally dissipated at other locations in physical space (Cimarelli *et al.* 2013).

The analysis of the reduced Yaglom equation, shown in figure 3(*d*) for $z^* = 0.5$, leads to similar conclusions. Both the inhomogeneous production Π^θ and the overall transport T_c^θ are dominant down to very small scales. A reverse cascade, $I_r^\theta < 0$, can be identified for separations $r_\rho^* \gtrsim 1.5$ due to the imbalance between the high production and the weak drain associated with transport and dissipation at scales less than r_ρ^*.

The complex picture emerging from the scale-by-scale analysis can be rationalized by isolating some fundamental regions inside the reduced (r_ρ^*, z^*) space. In light of the observations made in the previous few paragraphs, it is reasonable to split the separations into an inhomogeneity-dominated range at large r_ρ^* and a quasi-homogeneous range at small r_ρ^*, where the cross-over scales are denoted as ℓ_c^{u*} and $\ell_c^{\theta*}$, and satisfy the relations

$$\Pi^u(\ell_c^{u*}, z^*) + T_c^u(\ell_c^{u*}, z^*) = I_r^u(\ell_c^{u*}, z^*) + D_r^u(\ell_c^{u*}, z^*), \tag{3.3}$$

$$\Pi^\theta(\ell_c^{\theta*}, z^*) + T_c^\theta(\ell_c^{\theta*}, z^*) = I_r^\theta(\ell_c^{\theta*}, z^*) + D_r^\theta(\ell_c^{\theta*}, z^*). \tag{3.4}$$

While a direct cascade towards dissipation represents the fundamental mechanism for $r_\rho^* \lesssim \ell_c^{u*}$ and $r_\rho^* \lesssim \ell_c^{\theta*}$, the behaviour due the spatial inhomogeneity cannot be neglected for $r_\rho^* \gtrsim \ell_c^{u*}$ and $r_\rho^* \gtrsim \ell_c^{\theta*}$. Inside the inhomogeneous range, the joint action of production and overall transport in physical space actively modulates the transfer in space of scales leading to a reverse cascade. Hence, the additional scales ℓ_b^{u*} and $\ell_b^{\theta*}$, satisfying $I_r^u(\ell_b^{u*}) = 0$ and $I_r^\theta(\ell_b^{\theta*}) = 0$, can be introduced to mark the boundary between the direct cascade and the reverse cascade, completing a concise picture of the flow that accounts only for the most relevant processes.

The velocity and temperature characteristic scales are represented as a function of the wall distance in figure 4(*a*,*b*) for $Ra = 1.7 \times 10^5$, $Ra = 1.0 \times 10^6$ and $Ra = 1.0 \times 10^7$, where the Prandtl number is equal to 0.7. The supplementary datasets at lower Ra come from two DNS performed with the same numerical domain and boundary conditions as the main DNS at $Ra = 1.0 \times 10^7$. As shown in figure 4(*a*,*b*), the boundary scales between forward and reverse cascades, ℓ_b^{u*} and $\ell_b^{\theta*}$, exceed the corresponding cross-over scales between small homogeneous and large inhomogeneous scales, ℓ_c^{u*} and $\ell_c^{\theta*}$, at every wall distance. All the characteristic scales reach a minimum value in

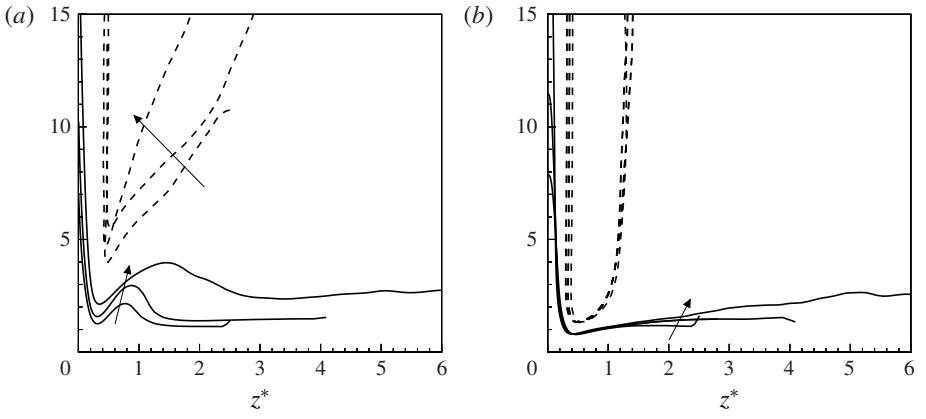

FIGURE 4. (*a*) Velocity cross-over scale ℓ_c^{u*} (solid lines) and boundary scale ℓ_b^{u*} (dashed lines), and (*b*) temperature cross-over scale $\ell_c^{\theta*}$ (solid lines) and boundary scale $\ell_b^{\theta*}$ (dashed lines) for $Ra = 1.7 \times 10^5$, $Ra = 1.0 \times 10^6$ and $Ra = 1.0 \times 10^7$, where the Rayleigh number increases in the direction of the arrows.

the near-wall region around $z^* \approx 0.2/0.6$, and then increase inside the viscous/diffusive layer. However, while ℓ_c^{u*} and $\ell_c^{\theta*}$ are defined along the entire domain, ℓ_b^{u*} and $\ell_b^{\theta*}$ are defined in a region close to the wall, where the reverse cascades occur.

Interestingly, the characteristic scales of the temperature are shown to be substantially *Ra*-independent while those of the velocity increase monotonically with the Rayleigh number. What we observe is due to the fact that the terms of the Yaglom equation do not change their shape with respect to r_ρ^* and z^*; hence the cross-over and boundary scales are unaltered by *Ra*. On the other hand, the Rayleigh number slightly modulates the shape of the Kolmogorov equation terms; thus ℓ_c^{u*} and ℓ_b^{u*} are *Ra*-dependent. In view of this, the smallest characteristic scale of the flow is imposed by the temperature field and it is equal to $\ell_{c,min}^{\theta*} \approx 0.8$ independently of the Rayleigh number. Moreover, we expect the temperature field to determine the minimum characteristic scale also for higher *Pr* due to the augmented separation between diffusive and viscous scales.

In the context of LES, the relative position of the filter length ℓ_F^* with respect to the cross-over scales is indicative of what mechanisms can be directly solved and what others should eventually be accounted for by an SGS model. If we consider a primary task to capture the large production and energy-containing scales, then the LES should employ filter lengths smaller than $l_{c,min}^{\theta*}$. Let us point out that such a constraint for the filter width is *Ra*-invariant; hence, it can be quantified *a priori* for different Rayleigh numbers and for a fixed Prandtl number, as long as an estimation of the Nusselt number is available (Grossmann & Lohse 2000). In accordance with the definition, for filter lengths smaller than $\ell_{c,min}^{\theta*}$, the unresolved mechanism that needs to be modelled is essentially the dissipation of turbulent kinetic energy and temperature variance; therefore, classic eddy-viscosity and eddy-diffusivity closures should be capable of providing good results. On the other hand, for filter lengths falling outside the homogeneous range, the physics captured by the LES is expected to be rather poor and the complexity of the phenomena occurring at subgrid level may bring some modelling issues. Regarding the latter point, an increase of the filter length beyond the boundary scales ℓ_b^{u*} and $\ell_b^{\theta*}$ could generate a net flux that originates at subgrid level to feed the larger resolved scales via a reverse cascade, as shown

by Cimarelli & De Angelis (2011) in the case of a turbulent channel flow. These conditions are a challenge for LES models, which should take into account strong backscatter effects (Cimarelli & De Angelis 2014).

4. Study of the filtered dataset

The filtering operation is a crucial stage in LES because it is conditioned by the fundamental and competing tasks of obtaining a reliable and accurate solution on the one hand, and to limit the computational expense on the other (Pope 2001). The choice of wide filter lengths allows computations to be performed on coarse grids and therefore it requires little computational resources; on the other hand, the physics resolved by the LES is quite poor and the solution strongly depends on the choice of the SGS model due to the large extent of the range of subgrid scales.

In order to disentangle the two distinct effects that the filtering operation has on the LES result, namely the degree of resolution of the actual dynamics and the influence of the modelling, a DNS dataset can be explicitly filtered to separate the resolved from the subgrid components of the different fields. This *a priori* approach has been pursued by many authors in order to compute quantities of interest, such as the equations for the filtered turbulent kinetic energy (Härtel *et al.* 1994), the filtered energy spectrum (Domaradzki *et al.* 1994) and the filtered scale energy (Cimarelli & De Angelis 2011).

The mathematical tools that we propose in this study are the filtered single-point budgets, equations (2.21) and (2.22), and their multiscale generalization, namely the filtered reduced Kolmogorov equation (2.14) and Yaglom equation (2.15). The filtered turbulent kinetic energy and temperature variance equations, to the authors' knowledge, have never been completely analysed in the case of RBC; thus § 4.1 has the purpose to present some results that are both novel and preparatory to the filtered multiscale analysis presented in the following sections, §§ 4.2 and 4.3. The DNS dataset at $Ra = 1.0 \times 10^7$ is split into resolved and subgrid components by applying a sharp cutoff filter in Fourier space in each of the wall-parallel directions, x and y, but not in the wall-normal direction, z (Domaradzki *et al.* 1994; Härtel *et al.* 1994). In what follows, the filtered budgets are analysed for filter lengths $\ell_F^* = (\pi H)/(\kappa_c Nu)$ ranging from 0.7 to 3.1, where κ_c is the cutoff wavenumber. This range of values has been chosen in order to analyse the behaviour of the resolved and subgrid velocity and temperature fields when the filter length is larger and smaller than the cross-over scales $\ell_{c,min}^{u*}$ and $\ell_{c,min}^{\theta*}$, respectively. We report the results for only two filter lengths, specifically $\ell_F^* = 1$ and $\ell_F^* = 3.1$ for the analysis of the velocity field, and $\ell_F^* = 0.7$ and $\ell_F^* = 2.1$ for the analysis of the temperature field. In terms of relative dimensions, the smallest filter width is comparable to the thickness of the thermal boundary layer ($\ell_F^* = 0.7$), whereas the largest one is slightly less than one-quarter of the height of the channel ($\ell_F^* = 3.1$). Let us note that the number of filter lengths that have been considered for this study is actually larger ($\ell_F^* = \{0.7, 1, 1.4, 2.1, 3.1, 5.1\}$), but these results are not shown for the sake of conciseness. However, the main differences will be specifically stated when relevant.

4.1. *Analysis of the filtered single-point budgets*

The main panels of figure 5(*a*,*b*) display the production of resolved turbulent kinetic energy, $\bar{\pi}^u$, and resolved temperature variance, $\bar{\pi}^\theta$, for two relevant filter lengths, together with their fully resolved counterparts, π^u and π^θ. It can be observed that the depletions of $\bar{\pi}^u$ and $\bar{\pi}^\theta$ with respect to the unfiltered terms can be

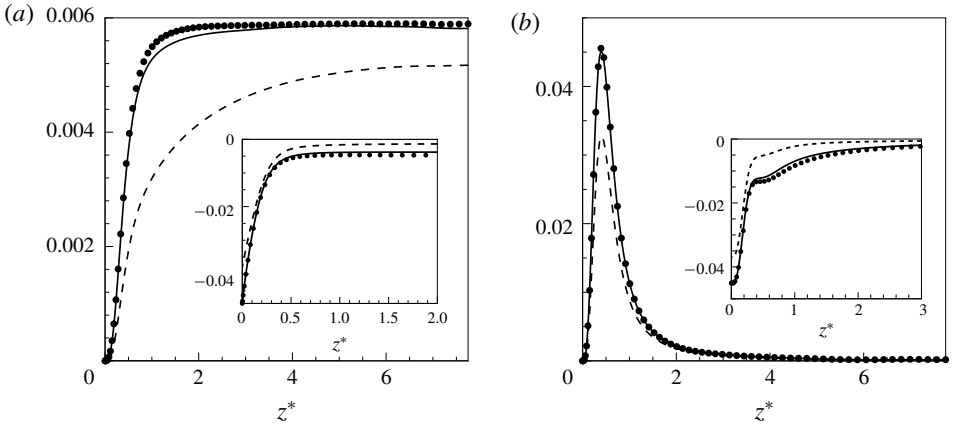

FIGURE 5. Unfiltered and resolved production of (a) the turbulent kinetic energy (circles for the unfiltered case, solid line for $\ell_F^* = 1.0$ and dashed line for $\ell_F^* = 3.1$) and (b) the temperature variance (circles for the unfiltered case, solid line for $\ell_F^* = 0.7$ and dashed line for $\ell_F^* = 2.1$). Insets: unfiltered and resolved dissipation of (a) turbulent kinetic energy and (b) temperature variance for the same filter lengths as the corresponding main panels.

considered negligible when the filter width falls inside the homogeneous range, i.e. $\ell_F^* < \ell_{c,min}^{u*} \approx 2.1$ and $\ell_F^* < \ell_{c,min}^{\theta*} \approx 0.8$, whereas they become important for large filter lengths. In particular, the difference between unfiltered and resolved productions is maximum in the near-wall region at $z^* \approx 1$ and $z^* \approx 0.5$; see figure 5(a) and 5(b), respectively. This behaviour is not surprising if we consider that the small scales that are filtered out produce mainly in the transitional layer rather than in other locations (see figure 3a–d); hence, the depletion that follows the filtering is expected to be more intense here than anywhere else.

The resolved dissipations $\langle\bar{\tilde{\epsilon}}\rangle$ and $\langle\bar{\chi}\rangle$ are affected by stronger depletions as larger filter lengths are employed, as can be seen from the insets of figure 5(a,b). Inside the bulk region, the resolved dissipations are negligible with respect to the fully resolved ones if the filter length is sufficiently larger than the minimum cross-over scales, which means that the subgrid scales are the only ones involved in dissipative mechanisms away from the wall. On the other hand, the resolved scales start to make an important contribution to the dissipation inside the transitional and viscous layers; indeed the ratios $\langle\bar{\tilde{\epsilon}}\rangle/\langle\tilde{\epsilon}\rangle$ and $\langle\bar{\chi}\rangle/\langle\chi\rangle$ have been found to increase monotonically as the wall is approached.

The different contributions to the overall transport of $\langle\bar{k}\rangle$ and $\langle\bar{\theta}^2\rangle$, namely the inertial, pressure and viscous transports of resolved turbulent kinetic energy and the inertial and viscous transports of resolved temperature variance, are represented in figure 6(a,b). As well as the resolved productions, the resolved transports overlap the unfiltered counterparts when $\ell_F^* < \ell_{c,min}^{\theta*}$ and $\ell_F^* < \ell_{c,min}^{u*}$ in accordance with the definition of the cross-over scales ℓ_c^{u*} and $\ell_c^{\theta*}$. The component that seems to be more affected by the increase of the filter length is the inertial transport, whereas the viscous and pressure contributions are barely depleted with respect to the unfiltered references. The inertial transports are negative inside the transitional layer, meaning that turbulent velocity and temperature fluctuations are carried away by inviscid mechanisms and swept towards the wall and towards the core.

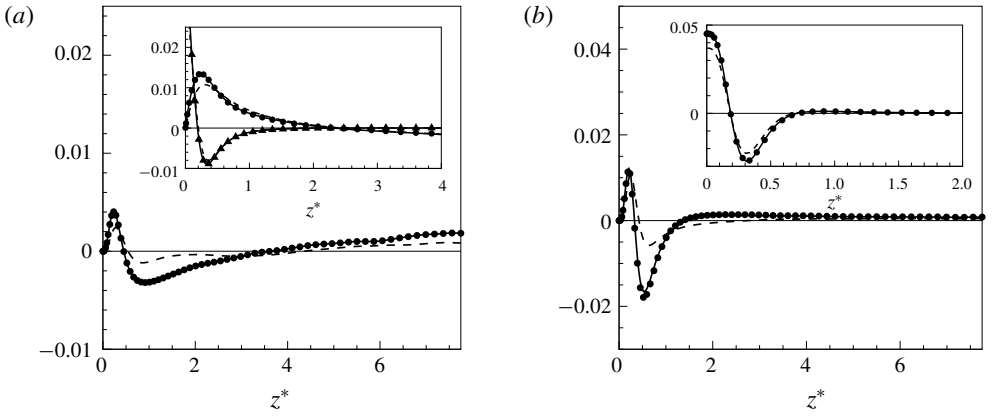

FIGURE 6. Unfiltered and resolved inertial transport of (*a*) the turbulent kinetic energy (circles for the unfiltered case, solid line for $\ell_F^* = 1.0$ and dashed line for $\ell_F^* = 3.1$) and (*b*) the temperature variance (circles for the unfiltered case, solid line for $\ell_F^* = 0.7$ and dashed line for $\ell_F^* = 2.1$). Insets: unfiltered and resolved (*a*) viscous and pressure transports of turbulent kinetic energy and (*b*) viscous transport of temperature variance for the same filter lengths.

The rates at which energy and temperature variance are extracted by inertial mechanisms inside the transitional layer are particularly affected by depletions. This behaviour could be reasonably explained in terms of the coherent structures that populate turbulent convection, i.e. the so-called thermal plumes. (See Togni *et al.* (2015) for a detailed analysis of thermal plumes conducted using the same DNS dataset as in the present work.) These structures, which have a diameter comparable with the thermal boundary layer thickness ($\delta_p^* \approx 0.5$), eject from the near-wall region and contribute significantly to the advective transport of turbulent kinetic energy and temperature variance towards the bulk. Hence, by filtering out the scales smaller than $\ell_F^* = 2.1$ or $\ell_F^* = 3.1$, we lose trace of the coherent modes of convection and a depletion of the inertial transport is somehow expected.

Let us now consider the average subgrid dissipations $\langle \epsilon_{sgs} \rangle$ and $\langle \chi_{sgs} \rangle$, represented as a function of z^* in the main panels of figures 7(*a*) and 7(*b*), respectively. Both terms are non-negative at every wall distance and for both large and small filter lengths, meaning that subgrid scales behave, on average, as sinks of turbulent kinetic energy and temperature variance. The shape of the profiles changes quite evidently passing from small to large filter lengths and this alteration is marked for $\langle \chi_{sgs} \rangle$, where a local minimum appears around $z^* = 0.5$. The only *a priori* calculation of subgrid dissipations in RBC known to the authors is the one by Kimmel & Domaradzki (2000) for $Ra = 6.3 \times 10^5$ and it shows a reasonable agreement with the present results.

The subgrid transports $t^u_{c,sgs}$ and $t^\theta_{c,sgs}$ can be considered negligible for $\ell_F^* < \ell_{c,min}^{u*}$ and $\ell_F^* < \ell_{c,min}^{\theta*}$, whereas they become relevant at large filter widths. In the latter case, the subgrid transports and the corresponding inertial transports have similar profiles, i.e. the subgrid scales, apart from extracting a net amount of turbulent kinetic energy and temperature variance from the resolved ones ($-\langle \epsilon_{sgs} \rangle < 0$ and $-\langle \chi_{sgs} \rangle < 0$), transport resolved fluctuations from the transitional layer towards the bulk and the near-wall region. It can be seen by comparing the main panels in figure 6(*a*,*b*) with the insets in figure 7(*a*,*b*) that the resolved inertial transport and the subgrid

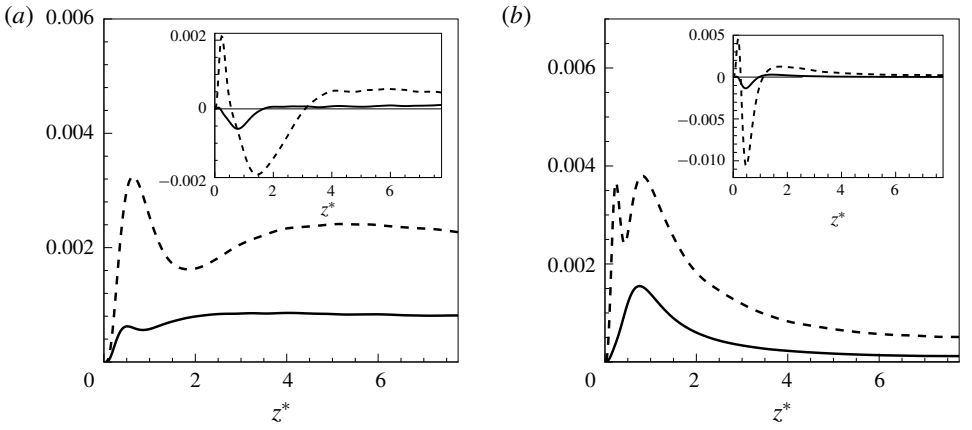

FIGURE 7. Profiles of subgrid dissipations (*a*) $\langle \epsilon_{sgs} \rangle$ and (*b*) $\langle \chi_{sgs} \rangle$ as a function of z^*, for $\ell_F^* = 1.0$ (solid line) and $\ell_F^* = 3.1$ (dashed line). Inset: profiles of SGS transport (*a*) $t^u_{c,sgs}$ and (*b*) $t^\theta_{c,sgs}$ as a function of z^*, for $\ell_F^* = 0.7$ (solid line) and $\ell_F^* = 2.1$ (dashed line).

redistribution terms are fairly comparable in magnitude inside the transitional layer, meaning that the nonlinear interactions between the resolved and the subgrid scales are as important as the ones between resolved scales. In terms of flow topology, this could be related to the nonlinear interactions between a hierarchy of structures living at subgrid level, namely the thermal plumes, and the large-scale circulation belonging to the resolved motion.

In closing this section, let us remark upon the role of the position of the filter length with respect to the characteristic scales ℓ_c^{u*} and $\ell_c^{\theta*}$. In accordance with their definition, the cross-over scales ℓ_c^{u*} and $\ell_c^{\theta*}$ split the spectrum of convective turbulence into a range of large scales, where the anisotropic production and inhomogeneous transport phenomena prevail, and a range of small scales, where turbulent cascade and dissipation processes dominate. This picture is also confirmed by considering low-pass-filtered velocity and temperature fields, since, as shown by the filtered single-point budgets analysed so far, the production and transports of turbulent kinetic energy and temperature variance are correctly reproduced by the filtered fields when $\ell_F^* < \ell_{c,min}^{u*}$ and $\ell_F^* < \ell_{c,min}^{\theta*}$. See appendix A for further details on the transition from well-resolved to poorly resolved physics.

4.2. *Analysis of the filtered reduced Kolmogorov equation*

In this section we analyse the filtered reduced Kolmogorov equation (2.14) at two distinct locations in physical space as representative of the scale-by-scale dynamics inside the bulk region and inside the transitional layer, and for two relevant filter lengths, $\ell_F^* = 1.0$ and $\ell_F^* = 3.1$, which are respectively smaller and larger than the minimum cross-over scale identified for the velocity field, $\ell_{c,min}^{u*} \approx 2.1$; see figure 4(*a*). The terms of the filtered budget are reported for $r_\rho^* \geqslant \ell_F^*$ to highlight that the range of scales for $r_\rho^* < \ell_F^*$ actually belongs to the subgrid motion. Indeed, for $r_\rho^* < \ell_F^*$, the terms of the filtered budget are still formally defined but, numerically, the only collocation point defined by the filtered resolution is located at the trivial separation, $r_\rho^* = 0$.

Figure 8(*a*,*b*) shows the budget in the bulk, $z^* = 3$, and in the transitional layer, $z^* = 0.7$, for the smallest filter length considered, $\ell_F^* = 1.0$. It can be seen that both

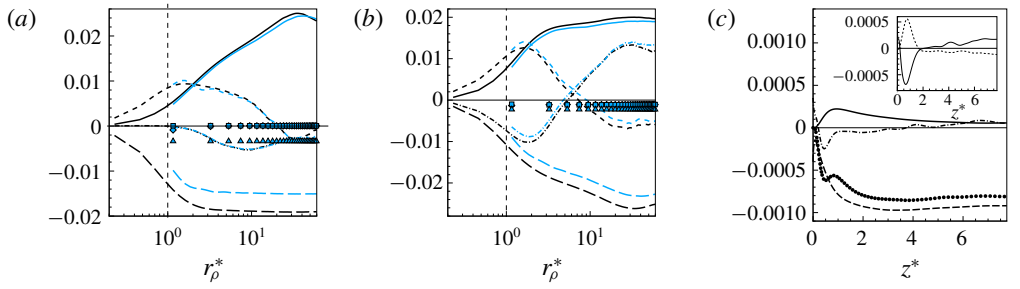

FIGURE 8. (Colour online) Scale-by-scale budgets (2.7) and (2.14) at (*a*) $z^* = 3$ and (*b*) $z^* = 0.7$ for $\ell_F^* = 1.0$. The unfiltered quantities are coloured black, the others are coloured blue (grey). Production (solid line), overall transport in physical space (dot-dashed line), transfer in the space of scales (dashed line), effective dissipation (long-dashed line), $T^u_{c,sgs}$ (squares), $T^u_{r,sgs}$ (diamonds), and E^u_{sgs} (triangles). The vertical dashed lines denotes ℓ_F^*. (*c*) Main panel: behaviour of $-\langle\epsilon_{sgs}\rangle$ (circles), $-\langle\tilde{\epsilon}'\rangle$ (long-dashed line), $t^{u'}_c - t^u_{c,sgs}$ (dot-dashed line) and $\pi^{u'}$ (solid line) as a function of z^* and for $\ell_F^* = 1.0$. Inset: profiles of $t^{u'}_c$ (solid line) and $-t^u_{c,sgs}$ (dashed line).

production and transport mechanisms are very well captured by the filtered fields, as the resolved terms $\bar{\Pi}^u$ and $\bar{T}_c{}^u$ fairly overlap the unfiltered counterparts, Π^u and T^u_c. This qualitative behaviour has been observed at every wall distance and agrees with the choice of a filter length that is small enough to fall inside the homogeneous range, where the net source/drain of energy due to the inhomogeneous production and overall transport is weaker than the direct cascade towards dissipation. In these conditions, a single physical phenomenon is filtered out, namely the action of viscosity at the smallest scales; indeed, a clear depletion of the effective dissipation is observed, $|\bar{E}^u_e| < |E^u_e|$. Accordingly, the unique role of the subgrid scales is to drain resolved energy, $E^u_{sgs} < 0$, as much as the missed dissipation due to resolved motion, i.e. the sum of the resolved and subgrid dissipations recovers the unfiltered dissipation, $\bar{E}^u_e + E^u_{sgs} \approx E^u_e$. The transports of resolved energy in physical and scale space due to the action of subgrid scales are, on the contrary, negligible, as $T^u_{c,sgs} \approx 0$ and $T^u_{r,sgs} \approx 0$.

For large filter lengths, we can observe a substantial change in the resolved dynamics. Figure 9(*a*) shows the scale-by-scale budget in the bulk of the flow at $z^* = 3$ and for $\ell_F^* = 3.1$. As we have $\ell_F^* > \ell^{u*}_{c,min}$, we expect a depletion of the effective amount of energy released at this wall distance by the production and transport mechanisms, i.e. $\bar{\Pi}^u + \bar{T}^u_c < \Pi^u + T^u_c$, in accordance with the definition of the cross-over scale $\ell^{u*}_{c,min}$. The inspection of figure 9(*a*) proves this expectation to be true and shows that the depletion is due only to the resolved production, $\bar{\Pi}^u < \Pi^u$, while $\bar{T}^u_c \approx T^u_c$. Also, the transport in the space of scales remains almost unaltered, $\bar{I}^u_r \approx I^u_r$, whereas the effective dissipation is drastically reduced, $|\bar{E}^u_e| \ll |E^u_e|$. Contrary to the previously shown cases where $\ell_F^* < \ell^{u*}_{c,min}$, now the effects of the SGS stresses on the resolved motion are no longer due to viscous mechanisms. Indeed, the net energy exchange between resolved and subgrid scales, E^u_{sgs}, is not given alone by the dissipation occurring at subgrid level but also by a non-negligible production. This fact leads to a value of the subgrid dissipation that is the balance between these two concurrent mechanisms; hence, it does not allow the unfiltered dissipation nor the unfiltered production to be recovered. Indeed, we found that the subgrid scales drain energy from the resolved ones without recovering the actual value of dissipation, i.e.

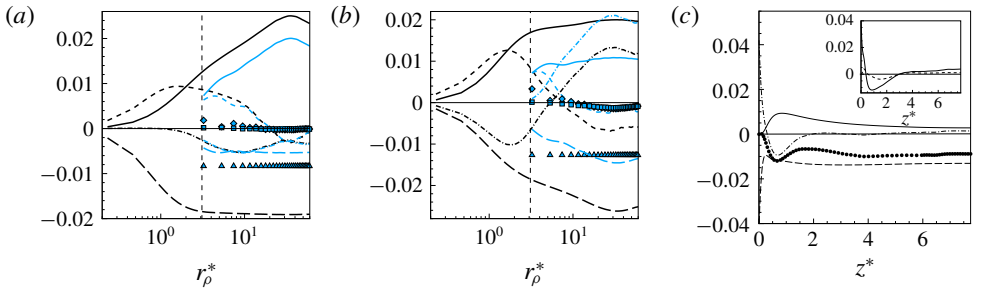

FIGURE 9. (Colour online) As figure 8 but for $\ell_F^* = 3.1$.

$|\bar{E}^u + E^u_{sgs}| < |E^u|$. Finally, the energy redistribution effect at resolved scales due to SGS stresses is found to be negligible in this region of the flow as $T^u_{c,sgs} \approx 0$ and $T^u_{r,sgs} \approx 0$.

Closer to the wall, inside the transitional layer at $z^* = 0.7$, we still observe an erosion of the real physics; see figure 9(*b*). However, contrary to the bulk region, not only a depletion of the production mechanisms is observed here, $\bar{\Pi}^u < \Pi^u$, but also a modification of the transports in physical and scale space becomes evident. In particular, we observe that the reverse energy transfer at large scales, $I^u_r < 0$, is not resolved, as $\bar{I}^u_r \approx 0$, while the forward cascade at small scales, $I^u_r > 0$, is partially recovered. This aspect suggests that the reverse cascade is a non-local phenomenon (in scale space) involving a wide range of scales, such that removing the eddies smaller than this filter length entails also a reduction of the transfer at large scales. The resulting depletion of the energy content of the large resolved scales is partially mitigated by an increase of the energy source due to the resolved spatial flux, since $\bar{T}^u_c > T^u_c$. Interestingly, the draining of the unfiltered spatial flux at small scales, $T^u_c < 0$, is not reproduced by the resolved motion. As shown in Togni *et al.* (2015), this double feature of the spatial flux is explained as a compound effect of spatial fluxes and reverse cascades. More explicitly, the presence of a reverse transfer in the space of scales deflects the spatial flux originating in the bulk so that in the transitional layer the large scales are gaining from the flux while small scales are still feeding the flux towards the wall. Since the reverse cascade occurring at large scale is not resolved for $\ell_F^* > \ell^{u*}_{c,min}$, the deflection of the spatial flux does not take place and, as a consequence, all the resolved scales gain energy from the bulk of the flow, $\bar{T}^u_c > 0$. A difference with respect to the bulk region is that now the SGS stresses contribute actively to the redistribution of resolved energy both in the physical space and in the space of scales, since the terms $T^u_{c,sgs}$ and $T^u_{r,sgs}$ are different from zero; see figure 9(*b*). The subgrid dissipation is negative, $E^u_{sgs} < 0$, as in the bulk of the flow; however, here E^u_{sgs} seems to take into account solely the missed dissipation at small scales, as $\bar{E}^u_e + E^u_{sgs} \approx E^u_e$.

To understand the mechanisms determining the observed behaviour of the subgrid dissipation, $E^u_{sgs} = -4\langle \epsilon_{sgs} \rangle$, we analyse in detail the equation for the subgrid turbulent kinetic energy $\langle k' \rangle = 0.5\langle u'_i u'_i \rangle$, namely

$$t^{u\prime}_c + \pi^{u\prime} - \langle \tilde{\epsilon}' \rangle - t^u_{c,sgs} + \langle \epsilon_{sgs} \rangle = 0, \tag{4.1}$$

where the terms denoted with the prime symbol and the ones without it in (2.17) are identical except for the replacement of velocity, temperature and pressure fields with

the subgrid counterparts. Since we consider a spectral cutoff filter, we have $\langle\bar{k}\rangle + \langle k'\rangle = \langle k\rangle$ and the sum of the subgrid and the resolved budgets corresponds to the unfiltered one.

Figure 8(*c*) shows the different terms of the budget (4.1) as a function of the wall distance and for $\ell_F^* = 1.0$. As can be seen from the main panel, the subgrid dissipation of resolved energy $\langle\epsilon_{sgs}\rangle$ is almost balanced by the viscous dissipation at subgrid level $\langle\tilde{\epsilon}'\rangle$ at every z^*. Indeed, the terms $t_c^{u\prime} - t_{c,sgs}^{u}$ and $\pi^{u\prime}$, which are respectively the global transport and production of subgrid turbulent kinetic energy, have a small magnitude with respect to $\langle\tilde{\epsilon}'\rangle$. These aspects support the previously mentioned single physical role of the subgrid stresses for $\ell_F^* < \ell_{c,min}^{u*}$, consisting of a drain of resolved energy due to viscous mechanisms. Although the sum $t_c^{u\prime} - t_{c,sgs}^{u}$ is lower in magnitude with respect to $\langle\tilde{\epsilon}'\rangle$, the separate contributions of the two transport terms, $t_c^{u\prime}$ and $-t_{c,sgs}^{u}$, shown in the inset of figure 8(*c*), while small throughout the bulk of the flow, become comparable to or even larger than $\langle\epsilon_{sgs}\rangle$ closer to the wall.

For large filter lengths, the mechanisms driving the subgrid dissipation E_{sgs}^{u} become more complex, as shown by figure 9(*c*) for $\ell_F^* = 3.1$. In the bulk region, the resolved energy released to the subgrid motion, $\langle\epsilon_{sgs}\rangle$, is balanced by viscous dissipation occurring at subgrid level $\langle\tilde{\epsilon}'\rangle$ minus the production of the unresolved scales $\pi^{u\prime}$, while $t_c^{u\prime} \approx 0$ and $t_{c,sgs}^{u} \approx 0$. The simplified relation $-\langle\epsilon_{sgs}\rangle \approx \pi^{u\prime} - \langle\tilde{\epsilon}'\rangle$ seems to be satisfied for $2 < z^* < 5$. Closer to the wall, for $z^* < 2$, the subgrid dissipation $\langle\epsilon_{sgs}\rangle$ is still driven by the dissipation and the production of subgrid scales; however, the global transport in physical space is increased in magnitude with respect to the deep bulk; it grows even more on approaching the wall and eventually balances the subgrid production around $z^* = 0.7$, thus explaining why $\bar{E}_e^{u} + E_{sgs}^{u} \approx E_e^{u}$ inside the transitional layer. It should be stressed that the subgrid dissipation E_{sgs}^{u} balances the residual dissipation $E_e^{u} - \bar{E}_e^{u}$ only in this case for $\ell_F^* > \ell_{c,min}^{u*}$, and that E_{sgs}^{u} is generally modulated by the inhomogeneous mechanisms taking place at subgrid level, namely the production and the transport of subgrid kinetic energy.

4.3. *Analysis of the filtered reduced Yaglom equation*

We proceed by analysing the filtered reduced Yaglom equation (2.15) inside the bulk, $z^* = 3$, and inside the transitional layer, $z^* = 0.4$, for the filter lengths $\ell_F^* = 0.7$ and $\ell_F^* = 2.1$, which are respectively smaller and larger than the smallest cross-over scale $\ell_{c,min}^{\theta*} \approx 0.8$; see figures 10(*a*,*b*) and 11(*a*,*b*). In the case $\ell_F^* < \ell_{c,min}^{\theta*}$, the resolved physics is very rich. As shown in figure 10(*a*,*b*), the production and transport mechanisms are captured well, $\bar{\Pi}^{\theta} \approx \Pi^{\theta}$, $\bar{T}_c^{\theta} \approx T_c^{\theta}$, and so is the transfer between scales, $\bar{I}_r^{\theta} \approx I_r^{\theta}$. The effect of the SGS heat flux is to drain temperature variance, $E_{sgs}^{\theta} < 0$, with negligible redistribution effects at resolved scales, since $T_{c,sgs}^{\theta} \approx 0$ and $T_{r,sgs}^{\theta} \approx 0$. Analogously to the velocity field, the condition $\ell_F^* < \ell_{c,min}^{\theta*}$ allows the main inhomogeneous processes to be resolved while leaving to the subgrid scales the duty of accounting solely for the diffusive mechanisms. Indeed, the rate at which temperature variance is drained by subgrid scales balances the missed dissipation at resolved scales, i.e. $\bar{E}_e^{\theta} + E_{sgs}^{\theta} \approx E_e^{\theta}$.

The picture changes when large filter widths are considered, as the resolved physics is strongly affected by the filtering operation and a significant portion of the relevant inhomogeneous mechanisms is left to be taken into account by the SGS heat flux. Accordingly, the scale-by-scale analysis for $\ell_F^* = 2.1$ reveals that $\bar{\Pi}^{\theta} + \bar{T}_c^{\theta} < \Pi^{\theta} + T_c^{\theta}$ both in the bulk and in the transitional layer; see figure 11(*a*,*b*). In particular, the production is adequately resolved in the bulk, where $\bar{\Pi}^{\theta} \approx \Pi^{\theta}$, but not inside the transitional layer. The reason is given by the fact that in the bulk region the

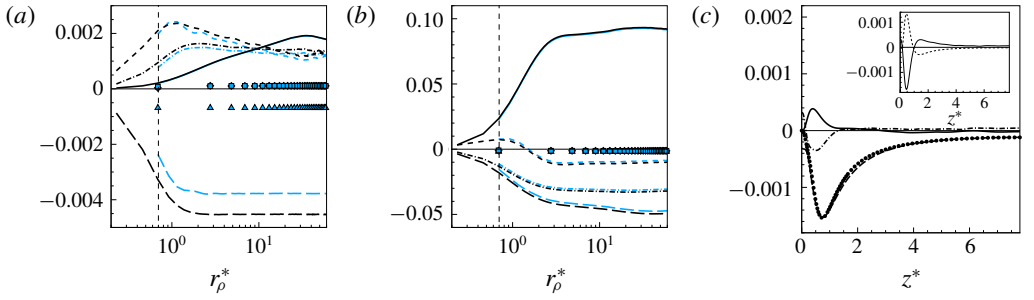

FIGURE 10. (Colour online) Scale-by-scale budgets (2.8) and (2.15) at (*a*) $z^* = 3$ and (*b*) $z^* = 0.4$ for $\ell_F^* = 0.7$. The unfiltered quantities are coloured black, the others are coloured blue (grey). Production (solid line), overall transport in physical space (dot-dashed line), transfer in the space of scales (dashed line), effective dissipation (long-dashed line), $T^\theta_{c,sgs}$ (squares), $T^\theta_{r,sgs}$ (diamonds), and E^θ_{sgs} (triangles). The vertical dashed lines denotes ℓ_F^*. (*c*) Main panel: behaviour of $-\langle\chi_{sgs}\rangle$ (circles), $-\langle\chi'\rangle$ (long-dashed line), $t_c^{\theta\prime} - t^\theta_{c,sgs}$ (dot-dashed line) and $\pi^{\theta\prime}$ (solid line) as a function of z^* and for $\ell_F^* = 0.7$. Inset: profiles of $t_c^{\theta\prime}$ (solid line) and $-t^\theta_{c,sgs}$ (dashed line).

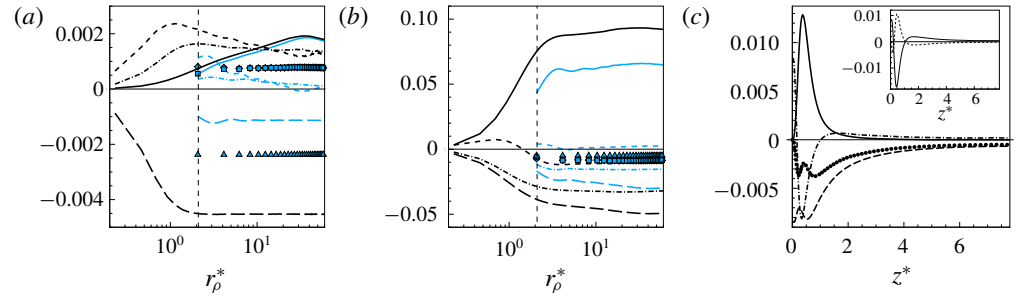

FIGURE 11. (Colour online) As figure 10 but for $\ell_F^* = 2.1$.

production processes are weak and involve large scales while in the transitional layer production is stronger and small scales are active in the relative mechanisms. Contrary to the production, the transport mechanisms are poorly resolved throughout the entire domain. Hence, the picture consists of resolved fields where the production of temperature variance in the transitional layer is deteriorated and, as a consequence, also the spatial flux that sustains the temperature fluctuations in the other regions of the flow is drastically reduced, i.e. $|\bar{T}^\theta_c| \ll |T^\theta_c|$. For the same reasons, also the resolved cascade mechanisms are strongly depleted, $|\bar{I}^\theta_r| \ll |I^\theta_r|$. As can be expected, this reduction of the forward and reverse transfers in the bulk and transitional layer, respectively, is more pronounced at large resolved scales where the intensity of these two resolved cascade phenomena is found to be almost null.

In agreement with these premises, the role of the SGS heat flux is relevant for the evolution of the resolved fields. In particular, the transport of resolved temperature variance in both physical and scale space is significantly determined by the interaction between resolved and unresolved scales, meaning that the subgrid redistributions $T^\theta_{c,sgs}$ and $T^\theta_{r,sgs}$ cannot be neglected. The net temperature variance exchange between resolved and subgrid scales is negative both in the bulk and in the transitional layer,

$E^{\theta}_{sgs} < 0$. However, this draining is not driven solely by diffusive mechanisms but also by inhomogeneous production and transport mechanisms, which are significant at subgrid level for large filter lengths. As a consequence, the subgrid dissipation does not allow one to recover the unfiltered rate of dissipation, i.e. $|\bar{E}^{\theta}_{e} + E^{\theta}_{sgs}| < |E^{\theta}_{e}|$.

In order to analyse in more detail the mechanisms determining the behaviour of the subgrid dissipation, $E^{\theta}_{sgs} = -2\langle\chi_{sgs}\rangle$, we analyse in detail the equation for the subgrid temperature variance $\langle\theta'^2\rangle$, namely

$$t^{\theta'}_{c} + \pi^{\theta'} - \langle\chi'\rangle - t^{\theta}_{c,sgs} + \langle\chi_{sgs}\rangle = 0, \tag{4.2}$$

where the terms denoted with the prime symbol and the ones without it in equation (2.18) are identical except for the replacement of velocity and temperature fields with the subgrid counterparts. Since we consider a spectral cutoff filter, $\langle\bar{\theta}^2\rangle + \langle\theta'^2\rangle = \langle\theta^2\rangle$ and the sum of the subgrid and the resolved budgets corresponds to the unfiltered one.

Figures 10(*c*) and 11(*c*) show the budget (4.2) for $\ell^{*}_{F} = 0.7$ and $\ell^{*}_{F} = 2.1$, respectively. In the case of $\ell^{*}_{F} < \ell^{\theta *}_{c,min}$ (see figure 10*c*), it can be seen that the subgrid dissipation is almost perfectly balanced by the viscous dissipation due to the subgrid scales, $\langle\chi_{sgs}\rangle \approx \langle\chi'\rangle$. The reason is that subgrid production, transport and the subgrid redistribution, $\pi^{\theta'}$, $t^{\theta'}_{c}$ and $-t^{\theta}_{c,sgs}$, are negligible inside the bulk of the flow. Closer to the wall, these terms become significant; however, they balance each other and thus they do not contribute to the subgrid dissipation. These results suggest that, for $\ell^{*}_{F} < \ell^{\theta *}_{c,min}$, the single relevant phenomenon that the SGS heat flux should take into account is the dissipation occurring at subgrid level. For this reason, as anticipated so far in the analysis of the scale-by-scale budgets, the combination of resolved and subgrid dissipation allows us to recover the unfiltered rate of dissipation, i.e. $\bar{E}^{\theta}_{e} + E^{\theta}_{sgs} \approx E^{\theta}_{e}$.

The picture becomes more complicated when large filter widths are considered. As can be seen in figure 11(*c*), the subgrid dissipation $\langle\chi_{sgs}\rangle$ not only is driven by $\langle\chi'\rangle$ but also is influenced by the subgrid production, transport and subgrid redistribution, in order $\pi^{\theta'}$, $t^{\theta'}_{c}$ and $-t^{\theta}_{c,sgs}$. In particular, in the bulk of the flow, subgrid production is negligible and subgrid dissipation is driven by the balance between spatial transport and dissipation at subgrid scales, $-\langle\chi_{sgs}\rangle \approx t^{\theta'}_{c} - t^{\theta}_{c,sgs} - \langle\chi'\rangle$. Close to the wall, also the production at subgrid scales becomes very significant; hence, it does contribute to the value of subgrid dissipation. In conclusion, for large filter lengths, subgrid scales are involved in strong inhomogeneous processes, so that subgrid dissipation does not take into account solely the dissipation at subgrid scales but also production and transport mechanisms. As a result, the sum of resolved and subgrid dissipation does not allow one to recover the unfiltered rate of dissipation, since $|\bar{E}^{\theta} + E^{\theta}_{sgs}| < |E^{\theta}|$ as previously shown in the analysis of the filtered Yaglom equation.

The analysis of the filtered dataset has important implications in LES. Classic eddy-viscosity/diffusivity models may provide a good estimation of the transfers between resolved and subgrid scales when $\ell^{*}_{F} < \ell^{\theta}_{c,min}$, as the main unresolved physics is the dissipation of turbulent kinetic energy and temperature variance. However, the inhomogeneous mechanisms become poorly resolved for larger filters and the SGS fields include highly dynamic eddies that contribute a significant portion of the production and transport besides dissipation, which may lead to modelling issues. Indeed, Smagorinsky-like models cannot account for the inhomogeneous mechanisms occurring at subgrid level; thus the exchanges between resolved and subgrid scales can hardly be copied.

Because the filtered Kolmogorov and the Yaglom equations have been proved to be of great support in describing the turbulent processes at different scales, locations in

physical space and filter lengths, then we might consider the filtered scale-by-scale analysis as a valuable tool for testing the SGS models that are commonly employed in LES. This idea has been conceived by Cimarelli & De Angelis (2012) and brought to a novel assessment of the SGS stress model in turbulent channel flow (Cimarelli & De Angelis 2014). Future works will continue this line of research and consider the possibility to employ the filtered Kolmogorov and Yaglom equations to evaluate the performances of the state-of-the-art models employed for thermally driven turbulence.

5. Conclusions

Turbulence is commonly described as being characterized by two different classes of processes: phenomena that occur in physical space, such as transport of momentum and energy, and phenomena that take place in the space of scales, such as the turbulent cascade. The dual nature of these two processes and of the related theories is a spurious result of the observables used to study turbulence. In the present work, we develop and assess an alternative formalism to overcome this scale/position duality. The theoretical framework is based on the equations for the velocity and temperature structure functions, the so-called generalized Kolmogorov and Yaglom equations (Togni *et al.* 2015). Such a framework is here extended for the assessment of convective turbulence when a low-pass filtering operation is used. The use of DNS data of turbulent Rayleigh–Bénard convection at $Ra = 1.0 \times 10^7$ and $Pr = 0.7$ finally allows us to prove the reliability of the developed theoretical framework for the study of the resolved and subgrid dynamics in thermally driven turbulence by varying the filter length.

We first use the Kolmogorov and Yaglom equations to define two physically relevant characteristic scales for the velocity and temperature fields. These scales, ℓ_c^u and ℓ_c^θ, respectively, decompose convective turbulence into a range of large scales, where anisotropic production and inhomogeneous spatial transports prevail, and a range of small scales, where, on the contrary, turbulent cascade and dissipation mechanisms dominate.

These cross-over scales are then used for a rational assessment of the resolved and subgrid dynamics of convective turbulence as a function of the filter length employed. In this context, the most severe constraint is given by the characteristic scale imposed by the temperature field, rather than by the velocity field, as the kinematic cross-over scale, ℓ_c^u, exceeds the thermal cross-over scale, ℓ_c^θ, at every wall distance and, arguably, for every Prandtl larger than 0.7, as the smallest temperature scale decreases when Pr increases. The analysis of the generalized Kolmogorov and Yaglom equations extended to filtered convective turbulence single out that, for filter lengths smaller than the cross-over scales (i.e. $\ell_F < \ell_{c,min}^\theta$, as $\ell_c^\theta < \ell_c^u$ everywhere), the resolved processes almost correspond to the exact ones except for a depletion of the resolved dissipations. In this case, the only role of the subgrid scales is to drain the amounts of energy and temperature variance that are not dissipated by resolved motion and temperature, that is to say, $E_{sgs}^u \approx E_e^u - \bar{E}_e^u$ and $E_{sgs}^\theta \approx E_e^\theta - \bar{E}_e^\theta$. On the other hand, when ℓ_F is sufficiently larger than $\ell_{c,min}^\theta$, a substantial fraction of the inhomogeneous range belongs to the subgrid scales; therefore, the physics of the flow is poorly resolved and the role of the subgrid scales is not only dissipative. With reference to the second issue, the exchanges of energy and temperature variance between resolved and subgrid scales, E_{sgs}^u and E_{sgs}^θ, are set by the unresolved dissipations plus the inhomogeneous processes occurring at subgrid level; hence, the recovery of the unfiltered dissipation, namely $E_e^u \approx \bar{E}_e^u + E_{sgs}^u$ and $E_e^\theta \approx \bar{E}_e^\theta + E_{sgs}^\theta$, does not occur in general.

Interestingly, the constraint given by the thermal cross-over scale non-dimensionalized with respect to twice the thermal boundary layer thickness, $\ell^{\theta *}_{c,min} = \ell^{\theta}_{c,min} Nu/H = 0.8$, is found to be substantially independent of the Rayleigh number, at least for the range of Ra considered in the present work. If confirmed, the developed criterion for the filter length would apply also for different Rayleigh numbers and fixed Prandtl number as long as an estimation of the Nusselt number is available.

As a final remark, let us point out that in the LES framework, the classic eddy-viscosity/diffusivity models should be capable of reproducing the subgrid dynamics for $\ell_F \approx \ell^{\theta}_{c,min}$, as the only physics that needs to be copied is the dissipation of turbulent fluctuations occurring at subgrid level. On the other hand, the classic SGS models arguably suffer some deficiencies close to the walls and for ℓ_F sufficiently larger than $\ell^{\theta}_{c,min}$, since they do not consider the mechanisms induced by spatial inhomogeneity, namely the subgrid production and transport in physical space. A future work will address both the *a priori* and *a posteriori* tests of classic SGS models in order to better assess the role of the filter length with respect to the cross-over scales of RBC and, eventually, to formulate a physics-based SGS model that is capable of accounting also for the inhomogeneous processes occurring at subgrid scales when large filter lengths are employed.

Appendix A. On the behaviour of the resolved energetics

Besides providing an exact theoretical framework for the study of the unfiltered, filtered and subgrid temperature and velocity fields both at the single-point and at the two-point level, the main body of the work makes use of the cross-over scales ℓ^{u}_{c} and ℓ^{θ}_{c} to assess the behaviour of the large-scale resolved fields as a function of the filter length ℓ_F employed. In particular, it is shown that for $\ell_F < \ell^{\theta}_{c,min}$, both the large-scale velocity and temperature fields essentially reproduce the unfiltered behaviours with the exception of a fraction of viscous dissipation, which might be easily reproduced by classical subgrid scale closures. It is then shown that for large filter lengths compared to the cross-over scale, of the order of $\ell_F \approx 3\ell^{\theta}_{c,min}$, the resolved physics is poor and subgrid-scale effects are more complex than a simple drain of kinetic energy and temperature variance, and thus challenging for turbulence closures. Hence, in the range $\ell^{\theta}_{c,min} < \ell_F < 3\ell^{\theta}_{c,min}$ the resolved field experiences a transition from a well-resolved to a poorly resolved physics. In this appendix, we provide additional details by addressing how this degradation of the resolved temperature and velocity fields occurs. To this purpose, we consider the behaviour of the production and spatial transport of turbulent kinetic energy and temperature variance as a function of the filter length employed, $\ell^{*}_{F} = \{0.7, 1, 1.4, 2.1, 3.1, 5.1\}$.

In figure 12(*a*), the behaviour of the production term of temperature variance is shown as a function of the filter length and for different wall distances, $\bar{\pi}^{\theta} = \bar{\pi}^{\theta}(z^*, \ell^*_F)$. The most evident depletion of resolved production occurs in the near-wall region, where most of the temperature variance is produced, while in the bulk region the isocontours are almost aligned in the vertical direction, thus denoting a weaker deterioration of production by increasing the filter length. This behaviour is reproduced by the cross-over scale $\ell^{\theta}_{c}(z^*)$. In particular, its minimum in the transitional layer, $\ell^{\theta *}_{c,min} = 0.8$, is found to nicely capture the largest filter length that can be adopted before the appearance of a deterioration of the resolved production. The same observations can be drawn by analysing the behaviour of the overall spatial transport $\overline{t}^{\theta}_{c}(z^*, \ell^*_F)$ shown in figure 12(*b*). Indeed, the peak of sink of temperature variance in the transitional layer which feeds the spatial transport towards the wall

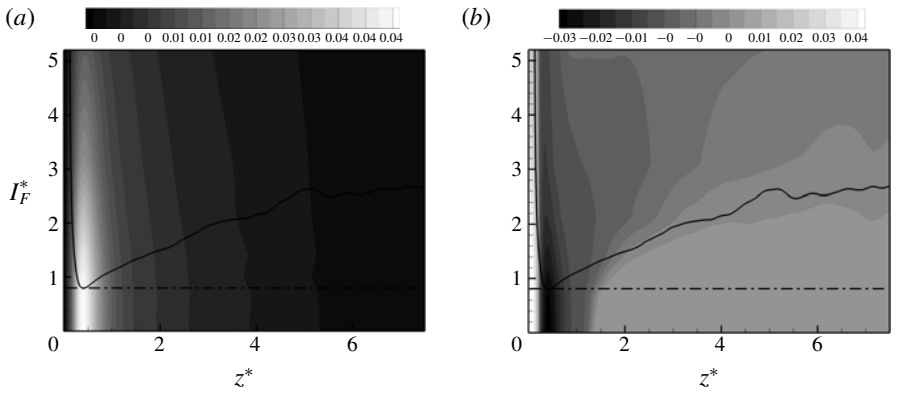

FIGURE 12. Intensities of the resolved temperature field processes as a function of the filter length and for different wall distances. (*a*) Production of temperature variance $\bar{\pi}^\theta(z^*, \ell_F^*)$. For $0 < \bar{\pi}^\theta(z^*, \ell_F^*) < 0.0025$, unequally spaced isocontours are used to address the behaviour of production also in the bulk of the flow. (*b*) Overall inhomogeneous transport $\bar{t}_c^\theta(z^*, \ell_F^*)$. For $-0.0025 < \bar{t}_c^\theta(z^*, \ell_F^*) < 0.0025$, unequally spaced isocontours are used to address the behaviour of transport also in the bulk of the flow. The solid line reports the behaviour of the cross-over scale $\ell_c^{\theta*}(z^*)$ while the dot-dashed line is the value of $\ell_{c,min}^{\theta*} = 0.8$.

and bulk regions is found to be significantly affected by the filter length. Again, this behaviour is nicely reproduced by the cross-over scale ℓ_c^θ, which is found to capture with its minimum, $\ell_{c,min}^{\theta*} = 0.8$, the maximum value of the filter length before the appearance of a deterioration of the negative peak of the spatial transport in the transitional layer. In contrast to the production term, the spatial transport shows a non-negligible filter length dependence also in the bulk of the flow. As highlighted by the isocontours, this dependence is such that the depletion of the spatial transport occurs at increasingly large filter lengths by increasing the distance from the wall. Also in this case, the cross-over scale ℓ_c^θ is found to nicely reproduce such behaviour.

Let us now consider the behaviour of the resolved turbulent kinetic energy. In figure 13(*a*), the behaviour of the resolved production of turbulent kinetic energy is shown again as a function of the wall distance and for different filter lengths, $\bar{\pi}^u = \bar{\pi}^u(z^*, \ell_F^*)$. In contrast to the temperature field, the production of turbulent kinetic energy is active in the bulk of the flow. This is the region where the effect of filtering is large while in the transitional and viscous layers it is very weak as highlighted by the progressive vertical alignment of the isocontours on decreasing the wall distance. In the bulk of the flow, the effect of filtering shows a dependence on the wall distance. In particular, the depletion of production occurs at increasingly large filter lengths on increasing the wall distance. Such behaviour is nicely captured by the cross-over scale $\ell_c^{u*}(z^*)$. In contrast to the bulk region, the transitional and viscous layers are dominated by the spatial transport $\bar{t}_c^\theta(z^*, \ell_F^*)$ as shown in figure 13(*b*). In particular, the maximum of the transport occurs in the viscous layer and the effect of filtering is not particularly significant, as shown by the almost vertical alignment of the iso-levels. The behaviour of the cross-over scale $\ell_c^{u*}(z^*)$ is found to correctly reproduce such a small dependence. Interestingly, the cross-over scale shows also a transition from the transport-dominated regions in the viscous and transitional layers to a production-dominated region in the bulk of the flow. This transition takes the

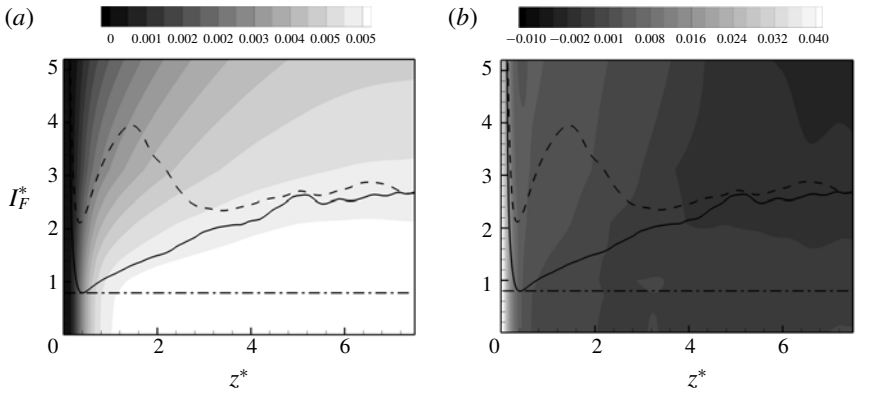

FIGURE 13. Intensities of the resolved velocity field processes as a function of the filter length and for different wall distances. (*a*) Production of turbulent kinetic energy $\bar{\pi}^u(z^*, \ell_F^*)$. (*b*) Overall inhomogeneous transport $\bar{t}_c^u(z^*, \ell_F^*)$. For $-0.007 < \bar{t}_c^\theta(z^*, \ell_F^*) < -0.002$, unequally spaced isocontours are used to address the behaviour of transport also in the bulk of the flow. The dashed line reports the behaviour of the cross-over scale $\ell_c^{u*}(z^*)$ while the solid line denotes $\ell_c^{\theta*}(z^*)$ as a reference. Also the value of $\ell_{c,min}^{\theta*} = 0.8$ is reported with the dot-dashed line.

form of a local maximum, thus denoting that the net compound role of production and transport in such a region involves larger scales.

In an LES context, the present results can be rationalized by using the behaviour of the cross-over scales. In particular, the temperature cross-over scale ℓ_c^θ, which is always smaller than that for the velocity field, $\ell_c^\theta < \ell_c^u$, is recognized to nicely mark the transition from well-resolved to poorly resolved temperature and velocity fields, as shown in figures 12 and 13. Furthermore, by considering the fact that the Rayleigh–Bénard problem is commonly solved by means of structured grids that are Cartesian in the wall-parallel planes (i.e. having constant spacing), the constraint given by $\ell_{c,min}^{\theta*}$, i.e. $\ell_F^* \leqslant \ell_{c,min}^{\theta*} = 0.8$, is recognized to identify a rule for the largest filter length that allows one to recover the unfiltered production and transport processes in the entire flow domain; see the horizontal dot-dashed line in figures 12 and 13. Let us finally remark that such a constraint is non-dimensionalized with respect to twice the thermal boundary layer thickness, $\ell_{c,min}^{\theta*} = \ell_{c,min}^\theta Nu/H = 0.8$, and, as shown in § 3, is found to be substantially independent of the Rayleigh number, at least for the range of *Ra* considered in the present work.

REFERENCES

AHLERS, G., BODENSCHATZ, E., FUNFSCHILLING, D., GROSSMANN, S., HE, X., LOHSE, D., STEVENS, R. J. A. M. & VERZICCO, R. 2012 Logarithmic temperature profiles in turbulent Rayleigh–Bénard convection. *Phys. Rev. Lett.* **109** (11), 114501.

ANTONIA, R. A. & ORLANDI, P. 2003 Effect of Schmidt number on small-scale passive scalar turbulence. *Appl. Mech. Rev.* **56** (6), 615–632.

BRYAN, G. H., WYNGAARD, J. C. & FRITSCH, J. M. 2003 Resolution requirements for the simulation of deep moist convection. *Mon. Weath. Rev.* **131** (10), 2394–2416.

BURATTINI, P., ANTONIA, R. A. & DANAILA, L. 2005 Scale-by-scale energy budget on the axis of a turbulent round jet. *J. Turbul.* (6), N19.

CABOT, W. H. 1993 Large eddy simulations of time-dependent and buoyancy-driven channel flows. *Annual Research Briefs 1992*. pp. 45–60. CTR Annual Research Briefs (Center for Turbulence Research, Stanford University/NASA Ames).

CHILLÀ, F. & SCHUMACHER, J. 2012 New perspectives in turbulent Rayleigh–Bénard convection. *Eur. Phys. J.* E **35** (7), 1–25.

CIMARELLI, A. & DE ANGELIS, E. 2011 Analysis of the Kolmogorov equation for filtered wall-turbulent flows. *J. Fluid Mech.* **676**, 376–395.

CIMARELLI, A. & DE ANGELIS, E. 2012 Anisotropic dynamics and sub-grid energy transfer in wall-turbulence. *Phys. Fluids* **24** (1), 015102.

CIMARELLI, A. & DE ANGELIS, E. 2014 The physics of energy transfer toward improved subgrid-scale models. *Phys. Fluids* **26** (5), 055103.

CIMARELLI, A., DE ANGELIS, E. & CASCIOLA, C. M. 2013 Paths of energy in turbulent channel flows. *J. Fluid Mech.* **715**, 436–451.

CIMARELLI, A., DE ANGELIS, E., JIMÉNEZ, J. & CASCIOLA, C. M. 2016 Cascades and wall-normal fluxes in turbulent channel flows. *J. Fluid Mech.* **796**, 417–436.

CORRSIN, S. 1951 On the spectrum of isotropic temperature fluctuations in an isotropic turbulence. *J. Appl. Phys.* **22** (4), 469–473.

DABBAGH, F., TRIAS, F. X., GOROBETS, A. & OLIVA, A. 2016 New subgrid-scale models for large-eddy simulation of Rayleigh–Bénard convection. *J. Phys. Conf. Ser.* **745** (3), 032041.

DABBAGH, F., TRIAS, F. X., GOROBETS, A. & OLIVA, A. 2017 A priori study of subgrid-scale features in turbulent Rayleigh–Bénard convection. *Phys. Fluids* **29** (10), 105103.

DANAILA, L., ANSELMET, F., ZHOU, T. & ANTONIA, R. A. 2001 Turbulent energy scale budget equations in a fully developed channel flow. *J. Fluid Mech.* **430**, 87–109.

DANAILA, L., KRAWCZYNSKI, J. F., THIESSET, F. & RENOU, B. 2012 Yaglom-like equation in axisymmetric anisotropic turbulence. *Physica D* **241** (3), 216–223.

DAVIDSON, P. A., PEARSON, B. R. & STAPLEHURST, P. 2004 How to describe turbulent energy distributions without the Fourier transform. In *Proceedings of the AFMC 15, Sydney, Australia*. University of Sydney.

DEARDORFF, J. W. 1974 Three-dimensional numerical study of the height and mean structure of a heated planetary boundary layer. *Boundary-Layer Meteorol.* **7** (1), 81–106.

DOMARADZKI, J. A., LIU, W., HÄRTEL, C. & KLEISER, L. 1994 Energy transfer in numerically simulated wall-bounded turbulent flows. *Phys. Fluids* **6**, 1583–1599.

DUPUY, D., TOUTANT, A. & BATAILLE, F. 2018 Turbulence kinetic energy exchanges in flows with highly variable fluid properties. *J. Fluid Mech.* **834**, 5–54.

GAUDING, M., WICK, A., PITSCH, H. & PETERS, N. 2014 Generalised scale-by-scale energy-budget equations and large-eddy simulations of anisotropic scalar turbulence at various Schmidt numbers. *J. Turbul.* **15** (12), 857–882.

GAYEN, B., HUGHES, G. O. & GRIFFITHS, R. W. 2013 Completing the mechanical energy pathways in turbulent Rayleigh–Benard convection. *Phys. Rev. Lett.* **111** (12), 124301.

GROSSMANN, S. & LOHSE, D. 2000 Scaling in thermal convection: a unifying theory. *J. Fluid Mech.* **407**, 27–56.

HÄRTEL, C., KLEISER, L., UNGER, F. & FRIEDRICH, R. 1994 Subgrid-scale energy transfer in the near-wall region of turbulent flows. *Phys. Fluids* **6** (9), 3130–3143.

HILL, R. J. 2002 Exact second-order structure–function relationships. *J. Fluid Mech.* **468**, 317–326.

KIMMEL, S. J. & DOMARADZKI, J. A. 2000 Large eddy simulations of Rayleigh–Bénard convection using subgrid scale estimation model. *Phys. Fluids* **12** (1), 169–184.

KOLMOGOROV, A. N. 1941*a* Dissipation of energy in locally isotropic turbulence. *Dokl. Akad. Nauk SSSR* **32**, 16–18.

KOLMOGOROV, A. N. 1941*b* The local structure of turbulence in incompressible viscous fluid for very large Reynolds numbers. In *Dokl. Akad. Nauk SSSR*, vol. 30, pp. 301–305. JSTOR.

LILLY, D. K. 1962 On the numerical simulation of buoyant convection. *Tellus* **14** (2), 148–172.

LILLY, D. K. 1967 The representation of small scale turbulence in numerical simulation experiments. In *Proceedings of the IBM Scientific Computing Symposium on Environmental Science*, pp. 195–210. IBM.

LIU, S., MENEVEAU, C. & KATZ, J. 1994 On the properties of similarity subgrid-scale models as deduced from measurements in a turbulent jet. *J. Fluid Mech.* **275**, 83–119.

LOHSE, D. & XIA, K.-Q. 2010 Small-scale properties of turbulent Rayleigh–Bénard convection. *Annu. Rev. Fluid Mech.* **42**, 335–364.

MARATI, N., CASCIOLA, C. M. & PIVA, R. 2004 Energy cascade and spatial fluxes in wall turbulence. *J. Fluid Mech.* **521**, 191–215.

MASON, P. J. 1989 Large-eddy simulation of the convective atmospheric boundary layer. *J. Atmos. Sci.* **46** (11), 1492–1516.

OBUKHOV, A. M. 1968 Structure of the temperature field in turbulent flow. *Tech. Rep.* DTIC Document.

PIOMELLI, U. 1999 Large-eddy simulation: achievements and challenges. *Prog. Aerosp. Sci.* **35** (4), 335–362.

PIOMELLI, U. & BALARAS, E. 2002 Wall-layer models for large-eddy simulations. *Annu. Rev. Fluid Mech.* **34** (1), 349–374.

PIOMELLI, U., CABOT, W. H., MOIN, P. & LEE, S. 1991 Subgrid-scale backscatter in turbulent and transitional flows. *Phys. Fluids* A **3** (7), 1766–1771.

POPE, S. B. 2001 *Turbulent Flows*. Cambridge University Press.

PORTÉ-AGEL, F., PARLANGE, M. B., MENEVEAU, C. & EICHINGER, W. E. 2001 A priori field study of the subgrid-scale heat fluxes and dissipation in the atmospheric surface layer. *J. Atmos. Sci.* **58** (18), 2673–2698.

SERGENT, A., JOUBERT, P. & LE QUÉRÉ, P. 2006 Large-eddy simulation of turbulent thermal convection using a mixed scale diffusivity model. *Prog. Comput. Fluid Dyn.* **6** (1-3), 40–49.

SIGGIA, E. D. 1994 High Rayleigh number convection. *Annu. Rev. Fluid Mech.* **26** (1), 137–168.

SMAGORINSKY, J. 1963 General circulation experiments with the primitive equations. 1. The basic experiment. *Mon. Weath. Rev.* **91** (3), 99–164.

TOGNI, R., CIMARELLI, A. & DE ANGELIS, E. 2015 Physical and scale-by-scale analysis of Rayleigh–Bénard convection. *J. Fluid Mech.* **782**, 380–404.

VALENTE, P. C. & VASSILICOS, J. C. 2015 The energy cascade in grid-generated non-equilibrium decaying turbulence. *Phys. Fluids* **27** (4), 045103.

VAN REEUWIJK, M., JONKER, H. J. J. & HANJALIĆ, K. 2005 Identification of the wind in Rayleigh–Bénard convection. *Phys. Fluids* **17** (5), 051704.

YAGLOM, A. M. 1949 On the local structure of a temperature field in a turbulent flow. *Dokl. Akad. Nauk SSSR* **69** (6), 743.